UC Santa Cruz

UC Santa Cruz Electronic Theses and Dissertations

Title
Dynamical Evolution of Dielectric Thin Film Interface Morphology Using a Phase-Field Method

Permalink
https://escholarship.org/uc/item/9d41x84n

Author
Sevic, John

Publication Date
2019

Peer reviewed|Thesis/dissertation

eScholarship.org Powered by the California Digital Library
University of California

UNIVERSITY OF CALIFORNIA
SANTA CRUZ

DYNAMICAL EVOLUTION OF DIELECTRIC THIN FILM INTERFACE MORPHOLOGY USING A PHASE-FIELD METHOD

A dissertation submitted in partial satisfaction of the
requirements for the degree of

DOCTOR OF PHILOSOPHY

in

ELECTRICAL ENGINEERING

by

John F. Sevic

June 2019

The Dissertation of John F. Sevic
is approved:

Professor Nobuhiko P. Kobayashi, Chair

Professor Sung-Mo (Steve) Kang

Professor Hongyun Wang

Lori G. Kletzer
Vice Provost and Dean of Graduate Studies

Copyright © by

John F. Sevic

2019

Table of Contents

List of Figures v

List of Tables x

Abstract xi

Dedication xii

Acknowledgments xiv

1 Introduction 1
- 1.1 Dielectric Thin Film Resistive Switching 1
- 1.2 Computational Formulation of Resistive Switching Phenomena 2
  - 1.2.1 Lumped Element Electrothermal Formulation 3
  - 1.2.2 Continuum Electrothermal Formulation 3
  - 1.2.3 Phase Field Formulation 4
- 1.3 Literature Benchmarking 7
- 1.4 Dissertation Contributions 7
- 1.5 Dissertation Organization 8

2 Multi-Physics Transient Simulation of Monolithic Niobium Dioxide-Tantalum Dioxide Memristor-Selector Structures 9
- 2.1 Introduction 9
- 2.2 Self-Consistent Transport Formulation 13
- 2.3 Simulation and Measurement Results 16
- 2.4 Discussion 18
- 2.5 Summary 24

3 Self-Consistent Continuum-Based Transient Simulation of Electroformation of Niobium Oxide-Tantalum Dioxide Selector-Memristor Structures 25
- 3.1 Introduction 25

3.2 Formulation of Equations of State 28
3.3 Discussion 33
3.4 Summary 40

4 A Computational Phase-Field Study of Possible Mechanisms of Conducting Channel Formation in Dielectric Thin Films 44
4.1 Introduction 44
4.2 Self-Consistent Phase-Field Formulation 49
4.3 Discussion 54
4.4 Summary 56

5 Conclusion and Future Directions 59

Bibliography 62

A Poole-Frenkel Conductivity Test Cases 73

B Phase Field Test Cases 76

C Multiphysics Object Oriented Simulation Environment - MOOSE 78

D MOOSE Isothermal Phase Field Source Code 96

E MOOSE Phase Field Isothermal Deck 103

List of Figures

1.1 The conducting channel formalism illustrated by a charged species cluster model. Panel (a) illustrates the pristine pre-formed state; panel (b) illustrates a possible formed state, showing one complete conducting channel forming a continuous path between the negative and positive contacts. The green circles represent discrete charged species, hosted by a dielectric, shown in tan. 5

1.2 Literature benchmarking comparing various capabilities of lumped element, continuum, and phase field formulations for the computational study of dielectric thin film resistive switching phenomena. Capabilities of the work produced in this dissertation are in the two right columns. . 6

2.1 Panel a) analytical TEM cross-sectional image of the self-assembled monolithically integrated NbO_2 selector self-aligned to a TaO_2 memristor after electroforming, with approximate locations of material boundaries. The TiN nano-via is 75 nm in diameter and is axially symmetric in the as-fabricated device (i.e. device before the electroforming). The Pt top layer is not shown. Panel b) measured electroforming I-V curves used for model calibration. The authors thank Dr. Kate J. Norris for helpful discussions on electroforming. 13

2.2 Equivalent planar representation of our axially-symmetric memristor-selector structure constructed by assuming there is no circumferential thermal or electric field component to the solution, state prior to electroforming. Ideal electrical and thermal insulating boundaries are assumed on the sides. The bottom W electrode is electrical ground and thermal ambient; the top Pt electrode is convectively coupled to ambient by a simple gap model and the electric potential is V_{form}. The TiN nano-via is 75 nm in diameter. The dashed vertical line centered on the x-axis denotes the cut-section for the temperature and electric potential shown by Figures 2.4 and 2.5 16

2.3 Steady-state thermal temperature for V_{form} = 1.3 V, illustrating a peak temperature in the thin-film stack of ≈ 1100 K and that substantial nano-via self-heating exists. The TiN nano-via is 75 nm diameter and the extent of the material on either side of the nano-via is also 75 nm, for a total width of the geometry of 225 nm. Perfect electrical and thermal insulators are assumed at the sides.The light dashed lines shows the approximate material boundaries; the image is cropped to the right to enhance detail of the selector-memristor structure and nano-via. 18
2.4 Steady state temperature, T, along the cut-section shown by the dashed vertical line in Figure 2.2. Temperature is shown for V_{form} = 1.3 V and V_{form} = 0.5 V. 19
2.5 Steady-state electric potential, V, along the cut-section shown by the dashed vertical line in Figure 2.2. Electric potential is shown for V_{form} = 1.3 V and V_{form} = 0.5 V. Note that the available electric field power is coupled in approximately equal proportion to the self-heating of the TaO_2 thin-film and TiN nano-via. 20
2.6 Instantaneous temperature T, at the top edge of the TaO_2 thin-film and the geometric center of the TiN nano-via, with V_{form} = 1.3 V. Instantaneous temperature of the TaO_2 thin-film is also shown for nonlinear electrical conductivity, illustrating NDR under transient electroformation. This simulation is denoted by NL, and represents the transient solution with electrical conductivity a function of T, described in Section III. 21
2.7 Lumped electrothermal equivalent parameters for thermal transient response model, illustrating substantial inhomogeneity.Note that conventional units for R and C are shown, however strictly speaking, the units are K/W and J/K, respectively. 22
2.8 Phase space representation of electroforming illustrating two different thermodynamical trajectories. Note that although both trajectories terminate at the same final state, the vastly different paths taken illustrates that different transport and emission phenomena are excited and that their order of excitation will influence the electroformed *i-v* characteristics of our selector-memristor structure in particular. 23

3.1 Equivalent planar representation of our axially-symmetric memristor-selector structure. The bottom W electrode is electrical ground and thermal ambient; the top Pt electrode is convectively coupled to ambient by a simple gap model and the electric potential is V_{form}. The sides are ideal electrical and thermal insulators. The circle indicates the physical coordinates for $\vec{r}$ for the evaluation of $T(\vec{r}, t)$ and $n(\vec{r}, t)$, local temperature and carrier density respectively. Chemical composition and thickness of each layer are shown. The diameter of the TiN nano-via is 75 nm. The dashed line immediately above the $TaO_{2.2}$ layer represents extent of the region discretized to undergo oxidation. 34

3.2 Transient response of instantaneous normalized resistivity following application of $V_{form} = 1.3$ V at $t = 0$ s. Resistance is normalized by the HR amorphous resistive state at $t = 0$ s. Creation of a continuum conducting region at the insulator-metal transition temperature of niobium oxide is illustrated by a ratio of the HR amorphous state resistance to the LR metallic state resistance greater than 20 dB. 36

3.3 Instantaneous temperature 0.95 ns following application of $V_{form} = 1.3$ V at $t = 0$ s; instantaneous temperature 50 ns following application of $V_{form} = 1.0$ V at $t = 0$ s; instantaneous temperature 50 ns following application of $V_{form} = 0.5$ V at $t = 0$ s. 42

3.4 Transient response of instantaneous temperature at the geometric center of the niobium oxide thin-film layer, following application of $V_{form} = 1.3$ V at $t = 0$ s. Instantaneous temperature is also shown for $V_{form} = 1.0$ V applied at $t = 0$ s and $V_{form} = 0.5$ V applied at $t = 0$ s. Note that electroforming and negative differential resistance obtain only for $V_{form} = 1.3$ V. Refer to Table II for a summary of transient response versus electric potential. 43

3.5 Phase-space dynamical evolution of Type I and Type II electroforming, with only two state variables shown, which could be, for example, applied electric potential and temperature at a geometric location in the (x, y)-plane of Figure 3.1.The idea represented by the diagram is that various trajectories of dynamical evolution are possible, depending on initial conditions, material composition and structure of a niobium oxide-tantalum dioxide selector-memristor. The final formed state, at T_{final}, occurs in a region of phase-space where desired performance obtains. In following with the phase-space diagram previously presented, it is important to note that various configurational and thermodynamic phases may be encountered by a specific trajectory. 43

4.1 The conducting channel formalism illustrated by a charged species cluster model. Panel (a) illustrates the pristine pre-formed state; panel (b) illustrates a possible formed state, showing one complete conducting channel forming a continuous path between the negative and positive contacts. The green circles represent discrete charged species, hosted by a dielectric, shown in tan. The phase field formulation tracks the dynamical evolution of the envelope of clusters of these charged species, whose interface collectively constitutes a conductive channel, subject to a variational principle and local conservation laws. 49
4.2 A pristine dielectric thin film structure composed of a conducting region and a non-conducting region to approximate an as-fabricated resistive switching device. The interface is represented by the dotted horizontal line, and is 4 nm from the bottom edge. The pristine concentration is established by an initial concentration, $c(\vec{r}, 0)$, uniformly distributed between 0.1 and 0.3 for the non-conducting state and 0.7 and 0.9 for the conducting state. The structure is 50 nm $\times$ 10 nm. 51
4.3 Initial state and the final state self-consistent solution of Equations 4.6a and 4.6b for concentration, $c(\vec{r}, t)$. The initial interface is formed 4 nm from the bottom contact. Panel (a) shows an ideal abrupt interface, defined as $c(\vec{r}, 0)$ being constant within the conducting and non-conducting regions, with panel (b) showing the resultant solution for $c(\vec{r}, t)$. The initial conditions of this abrupt interface are established by uniformly setting the conducting and non-conducting concentrations of the structure to 0.7 and 0.3, respectively. In this case, no conducting channel growth was observed, suggesting formation of conducting channels that bridge the top and bottom contacts is not energetically favored if the initial interface is abrupt. Panel (c) shows a diffuse interface, established by an initial concentration, $c(\vec{r}, 0)$, uniformly distributed between 0.1 and 0.3 for the non-conducting state and 0.7 and 0.9 for the conducting state, reproducing the pristine thin-film structure shown in Figure 4.2. Panel (d) showing the resultant solution for $c(\vec{r}, t)$, showing formation of several conducting clusters and one continuous conducting channel, distinguished by the conducting domains shown in red and the non-conducting domains shown in blue. Panel (e) applies the initial conditions of panel (c) to a 50 nm $\times$ 50 nm structure, with the resultant solution for $c(\vec{r}, t)$ shown by panel (f). It is evident that while formation of several conducting channel-like clusters has occurred, there does not appear to be a continuous conducting channel traversing the bottom edge to the top edge of the thin film structure. 58

A.1 Continuum test case of Poole-Frenkel conductivity versus square root of electric field. 74

A.2 Continuum test case of Poole-Frenkel conductivity versus inverse of temperature. 75

B.1 Phase field test cases to validate electrostatic potential term. 77

List of Tables

2.1 Material and geometry parameters used for simulation. 17

3.1 Material description, layer thickness, and width of equivalent planar representation of our axially-symmetric memristor-selector structure constructed by assuming zero circumferential thermal or electric field component. Specific details of the 2-D equivalent selector-memristor structure were previously published. 30

3.2 Transient response comparison for various V_{form}. Maximum temperature, T_{max}, is defined as peak temperature at the geometric center of the niobium oxide thin-film layer. Rise time, t_{rise} is defined as the time from 10% to 90% of the steady-state value. Steady-state conditions, t_{steady} and T_{steady}, , are defined as within 1% of the final value, as determined by the MOOSE solver. 39

Abstract

Dynamical Evolution of Dielectric Thin Film Interface Morphology Using a Phase-Field Method

by

John F. Sevic

A phase field method is used to computationally study conducting channel morphology of resistive switching thin film structures. Our approach successfully predicts the formation of conducting channels in typical dielectric thin film structures, comparable to a range of resistive switches, offering an alternative computational formulation based on metastable states treated at the atomic scale. In contrast to previous resistive switching thin film models, our formulation makes no *a priori* assumptions on conducting channel morphology and its fundamental transport mechanisms.

In memory of Agatha Zaidel-Sevic and Makoto Shichida.

Homo liber nulla de re minus quam de morte cogitat; et ejus sapientia non mortis sed vitae meditatio est. **SPINOZA'S** *Ethics*, Pt. IV, Prop. 67

Acknowledgments

I would like to thank the fantastic instructors I had during my time at Santa Cruz, particularly Dr. Josh Deutsch for solid-state and Dr. Toshinege Yamada for quantum, each providing a challenging and enriching learning environment. High-speed devices with Dr. Steve Kang was a blast, and the Bell Labs stories were priceless. Perturbation theory with Dr. Hongyun Wang is about as close I will get to being musical, an extremely enriching and practical class for my research. I also would like to thank my Preliminary Exam committee, composed of Dr. Josh Deutsch, Dr. Steve Kang, Dr. Hongyun Wang, and my Advisor, Dr. Nobuhiko Kobayashi; I also thank my Defense Committee, composed of Dr. Steve Kang, Dr. Hongyun Wang, and my Advisor, Dr. Nobuhiko Kobayashi.

Many thanks go to my Advisor, Dr. Nobuhiko Kobayashi, for his expert coaching, guidance, and vision. Many times I felt like Dante lost in the wood, going in circles on some of those circles, only to come back out into an opening with clarity and understanding that I did not believe possible. I will forever relish our talks and discussions.

Chapter 1

Introduction

1.1 Dielectric Thin Film Resistive Switching

Resistive switching phenomena are currently being explored as a fundamental technology for next-generation non-volatile memory applications. Incumbent non-volatile memory technology subjects charge transport and storage to quantum-scale effects, manifested as power consumption and heat, while in contrast information storage by resistive switching obtains by modulation of the bulk conductivity of a dielectric thin film. Two attractive features of resistive switching non-volatile memory technologies are substantial reductions in power consumption and scaling beyond incumbent Moore-limited transistor-based memory-cells[1].

Appropriately prepared resistive switching dielectric thin films exhibit a desirable characteristic hysteresis, central to their operation as next-generation non-volatile memory technology, due to various underlying physical mechanisms, such as insulator-

metal phase transition (IMT). Insulator-metal phase transition is itself a consequence of intrinsic metastable atomic states of thin film materials and controlled introduction of irreversible states endowed by specific preparation processes. Resistive switching phenomena viewed from these various physical abstractions - atomic, molecular, and continuum - suggests a rich spectrum of computational formulations to study the dynamical behavior of resistive switching dielectric thin films and their performance as a fundamental memory technology.

The objective of the present dissertation is to explore various computational formulations to study the dynamical behavior of resistive switching dielectric thin films. The study begins with a self-consistent continuum transient formulation of electroformation of niobium oxide-tantalum dioxide memristor-selector structures based on Poole-Frenkel defect transport. A phase field method is next developed to computationally study conducting channel morphology of resistive switching dielectric thin films. This approach successfully predicts the formation of conducting channels in typical dielectric thin films, comparable to a range of resistive switch structures for next-generation non-volatile memory applications.

1.2 Computational Formulation of Resistive Switching Phenomena

This section reviews various computational formulations for the study of the dynamical behavior of resistive switching dielectric thin films.

1.2.1 Lumped Element Electrothermal Formulation

A lumped element formulation, *e.g.* an equivalent circuit model, is a simple and effective method to self-consistently formulate electrothermal behavior of memristive thin film behavior[2]. By adopting specific closed-form for ionic transport phenomena, such as Poole-Frenkel transport self-consistently coupled with instantaneous temperature, electrothermal effects such as insulator-metal transition can be simulated. However, because the model is essentially a point, it does not resolve the inhomogeneity and 3-D effects intrinsic to dielectric thin film resistive switching phenomena.

1.2.2 Continuum Electrothermal Formulation

Self-consistently coupling of the conservation equations representing various transport phenomena associated with dielectric thin film resistive switching phenomena is an effective and powerful method to study both the steady-state and transient behavior of such structures. For example, Nardi self-consistently coupled Poole-Frenkel transport, thermal transport, and charge conservation to model the steady-state *i-v* behavior of their memristor structure[3] [4]. Kim also posed a similar formulation[5]. The work of Nardi and Kim is reviewed extensively in Chapters Two and Three. Diaz performed an initial computational study of Joule heating of niobium oxide-tantalum dioxide memristor-selector structures [6]'[7]. The Diaz work was subsequently extended by the present dissertation for the computational transient study of electroformation of niobium oxide-tantalum dioxide memristor-selector structures[8][9].

1.2.3 Phase Field Formulation

In contrast with the lumped equivalent and continuum formulations, various qualitative models have been adopted to study resistive switching behavior of dielectric thin films, largely based on formation of so-called conducting channels composed of clusters of charged species[10],[11],[12],[13]. These models invoke both electronic transport and ionic transport, often treated as electrothermal and electrochemical processes, respectively, reproducing both unipolar and bipolar resistive switching behavior. The conducting channel formalism suggests an initial irreversible growth of cluster-like aggregates composed of charged species forming conducting channels, as illustrated by Figure 1.1. These conducting channels subsequently form and rupture under the influence of an external electric potential, yielding resistive switching behavior.

Self-consistent solution of the continuum transport equations dynamically emulates advection and diffusion of thermally-activated charged species, and their interaction with local electric potential and temperature, to model bulk resistive switching phenomena. The continuum formulation, however, depends vitally on an *a priori* conducting channel transport model and correct identification of diffusion and mobility expressions for each specific transport mechanism, for example Poole-Frenkel transport for ionic vacancy conduction[2],[9],[8],[3],[4],[5],[14],[15].

A computational formulation that does not *a priori* impose assumptions on conducting channel morphology, transport phenomena, or interface uniformity, and instead treats resistive switching from its origin at the atomic-scale, may offer significant

advantages over existing methods. Such a method might model the dynamical evolution of cluster-like charged aggregates, as illustrated by Figure 1.1, subject to their atomic and interfacial electrothermal interaction, naturally producing conducting channels in a non-conducting host. The phase field method is one such method[16],[17],[18],[19].

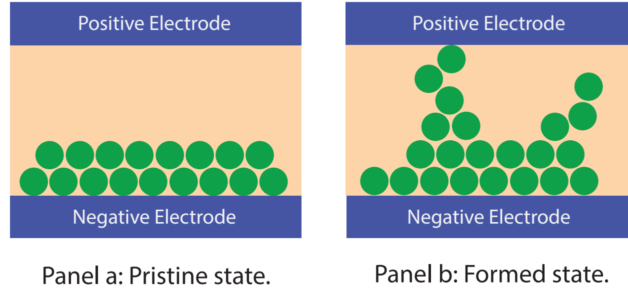

Figure 1.1: The conducting channel formalism illustrated by a charged species cluster model. Panel (a) illustrates the pristine pre-formed state; panel (b) illustrates a possible formed state, showing one complete conducting channel forming a continuous path between the negative and positive contacts. The green circles represent discrete charged species, hosted by a dielectric, shown in tan.

With the phase field formualtion, the assumptions of an *a priori* conducting channel model and the presence of specific transport phenomena to explain resistive switching are abandoned, and the model is instead formulated as a diffuse interface problem subject to a variational principle[20]. The phase field formulation thus avoids the mathematically onerous problem of expressing dynamic boundary conditions over an interface whose location is part of the unknown solution.

As demonstrated by the present dissertation, the phase field formulation successfully predicts the formation of conducting channels in typical dielectric thin films comparable to a range of resistive switch structures, offering an alternative computa-

tional formulation based on metastable states treated at the atomic scale, requiring no assumptions on conducting channel morphology and its fundamental transport mechanisms. The approach applies to both electronic transport and ionic transport, *e.g.* ionic oxygen vacancies.

Capability	Published Lumped Element	Published Continuum	This Dissertation	
			Continuum	Phase-Field
Self-Consistent Electrothermal Transport	Assumed Ideal	Yes	Yes	Yes
Self-Consistent Charge Transport	Assumed Ideal	Yes	Yes	Yes
Conductivity from First Principles	No	Yes	Yes	Yes
Continuum Phase Change Formulation	No	Yes	Yes	Yes
Atomic-Origin Phase Change Formulation	No	No	No	Yes
Scales to Nanoscale Transport	No	Assumed	Assumed	Yes
Transient Dynamics	Yes	Yes	Yes	Yes
Electroforming Dynamics	No	No	Yes	Yes
Conducting Channel Morphology and Growth	No	No	No	Yes

Figure 1.2: Literature benchmarking comparing various capabilities of lumped element, continuum, and phase field formulations for the computational study of dielectric thin film resistive switching phenomena. Capabilities of the work produced in this dissertation are in the two right columns.

1.3 Literature Benchmarking

Figure 1.2 immediately above shows a qualitative comparison of the various computational formulations surveyed in this introductory review. It is evident that to the user of the phase field formulation accrues many benefits favorable to the study of the dynamical behavior of dielectric thin film resistive switching phenomena.

1.4 Dissertation Contributions

The contributions of the present dissertation were stimulated by discussions with the author's Advisor, Dr. Nobuhiko Kobayashi, on the formulation and solution of Stefan-like dynamic interface boundary-value problems and how these methods could be applied to simulate conducting channel formation in appropriately prepared dielectric thin films. Experimental data suggested that clusters of charged species formed conducting channels, as illustrated by Figure 1.1, whose aggregate behavior represents the dynamical evolution of an interface under the influence of an external forcing function, *e.g.* an electric field, subject to local conservation laws. Computational analysis of the dynamical evolution of dielectric thin film resistive switching conducting channel formation using a phase field formulation is the fundamental contribution of this dissertation.

The following list tabulates the primary contributions of this dissertation.

- Demonstration of a phase field method as a fundamental computational tool for the study of dielectric thin film resistive switching phenomena

- Phase field computational solution of the dynamical evolution of an interface to model conducting channel formation of resistive switching dielectric thin films
- Self-consistent continuum transient simulation of electroformation of niobium oxide-tantalum dioxide memristor-selector structures based on Poole-Frenkel transport
- Self-consistent continuum transient simulation of Joule heating of niobium oxide-tantalum dioxide memristor-selector structures

1.5 Dissertation Organization

There are five chapters, with the first and last chapters being the customary introduction and abbreviated literature review, and, conclusion and future directions, respectively. The remaining three primary chapters represent the primary research produced by this dissertation, each representing a distinct publication. There are five appendices, providing additional details on simulation test cases and the simulation environment.

Chapter 2

Multi-Physics Transient Simulation of Monolithic Niobium Dioxide-Tantalum Dioxide Memristor-Selector Structures

2.1 Introduction

Memristive memory cells, referred to as memristors, are one of many emerging logic technologies offering quasi-classical physical scaling at the nanoscale, with necessary yield for high-volume fabrication of next-generation resistive random-access memory (RRAM) structures and related elements, such as neuromorphic cores[14][21][22][23]. Reduced to practice, however, for example in the cross-bar array, the memristor read-write *i*-*v* trajectory requires augmentation by a selector element to reduce spurious coupling between adjacent memory cells. Selector elements based on negative differential resistance (NDR) exhibit a highly desirable nonlinear *i*-*v* trajectory that sub-

stantially suppresses spurious triggering of adjacent memory cells. Both current-and voltage-controlled NDR can be manifested by a broad variety of physical phenomena, including thermionic emission, quantum tunneling, and insulator-to-metal phase transition of many binary oxides. Because of the ease of serial monolithic integration with an associated memristor cell, two-terminal thin-film selector elements are being fabricated by various research groups[24][6][7], since such structures natively integrate with standard memory and logic flows.

Various computational methods have been proposed to explain both electroformation, which remains largely an empirical process, and the associated selector-memristor two-terminal *i-v* trajectory. For example, Chang *et al.* performed a computational study of Joule heating in NiO_2 thin-film memristors, showing good agreement with their measurements [25]. Their measured data also showed that the steady-state temperature of NiO_2 bulk was approximately equal to the insulator-to-metal transition temperature (IMT). Noman *et al.* developed a novel pulsed *i-v* measurement system to extract the thermal time constant of a TaO_2 thin-film memristor electroformed by Joule heating [26]. By self-consistently coupling thermal and electron transport, the simulated electroforming thermal time constant showed good agreement with their measurement. Nardi and Larentis presented a self-consistent treatment of the influence of ionic defect transport on the *i-v* trajectory of TaO_2 thin-film memristors, under the assumption of the presence of a quasi-static current filament [3] [4]. Their work showed good agreement between measured and simulated *i-v* trajectories based on their current filament model [4]. Kim also showed a similar method to that of Nardi [5]. Cassidy *et al.* demon-

strated memristive behavior of TaO_2 thin-films using a Nernst-Planck mass transport formulation, illustrating ionic defect mass transport as a primary factor of memristor *i-v* hysteresis [27]. Gibson *et al.* demonstrated NDR in NbOx thin-film selectors using a compact behavioral model self-consistently coupled to a Joule self-heating network [2]. The results suggest that NDR obtains due to Poole-Frenkel ionic defect transport at a selector bulk temperature substantially less than the IMT temperature of NbO_x. Nandi *et al.* have recently demonstrated a computational study of HfO_2-based RRAM structures indicating that electroforming compliance influences selector-memristor behavior [28].

The present computational study was motivated by several key experimental implications obtained by fabricating and characterizing our NbO_2-TaO_2 selector-memristor devices [24][6][7]. The as-fabricated devices were grown on a Si (100) substrate, with the material stack-up shown in Figure 2.1. The substrate was ultrasonically cleaned with acetone and isopropyl alcohol, then reactive ion etched with oxygen plasma for 30 s and finally ion milling etched at 400 W in argon gas for 90 s prior to the bottom electrode deposition. The TiN nano-via is surrounded by SiO_2 and Si_3N_4 isolation layers. A $TaO_{2.2}$ switching layer was deposited by reactive RF sputtering using a $TaO_{2.2}$ target with an argon gas flow of 273 sccm and an oxygen gas flow of 77 sccm. Metallic Nb and Pt top electrode layers were defined by shadow masks and deposited by electron beam deposition at ambient temperature to thicknesses at a chamber pressure of 2.2 μTorr and a growth rate of 0.1 nm/s. Measured *i-v* data were obtained from an Agilent 4156C parameter analyzer. Bias voltage was applied to the Pt top electrode with the W

bottom electrode grounded. For the electroformation presently considered, simulation parameters were extracted based on the measured set and reset currents of $\approx$ 10 mA and $\approx$ 10 μA, respectively, as illustrated by the measured data of Figure 2.1.

Our simulation results illustrate the electroformed NbO_2 thin-film bulk reaches a temperature comparable to the IMT of 1081 K, based on simulated current of $\approx$10 mA, forming the basis of the present transient simulation [6]. While a compact model formulation can resolve quasi-static bulk two-terminal selector-memristor *i-v* characteristics of idealized effects, a first-principles formulation based on coupled transport phenomena offers a non-equilibrium picture of the thermodynanmical evolution of electroforming and memristor *i-v* characteristics *ab initio*. This framework provides physical insight on the interaction of arbitrary mass transport phenomena, such as Poole-Frenkel ionic defect hopping, coupled to electrothermal transport, evolving self-consistently in time. This additional sophistication enables, for example, electroformation simulation of nano-via properties on selector-memristor behavior.

In this paper, we present a computational study of a monolithically integrated self-assembled NbO_2 thin-film selector element self-aligned to a TaO_2 memristor, illustrated by a cross-sectional transmission electron microscope (TEM) image in Figure 2.1. Our TEM-based chemical analysis suggests that by careful electroforming, thermodynamically preferential oxidation of Nb present in close proximity to the TaO_2 yields a self-aligned NbO_2 thin-film selector element at the NbO_2-TaO_2 interface. Our computational results show that the electroformed NbO_2 bulk temperature reaches the IMT of 1081 K, in support of our theory suggesting phase change due insulator-metal

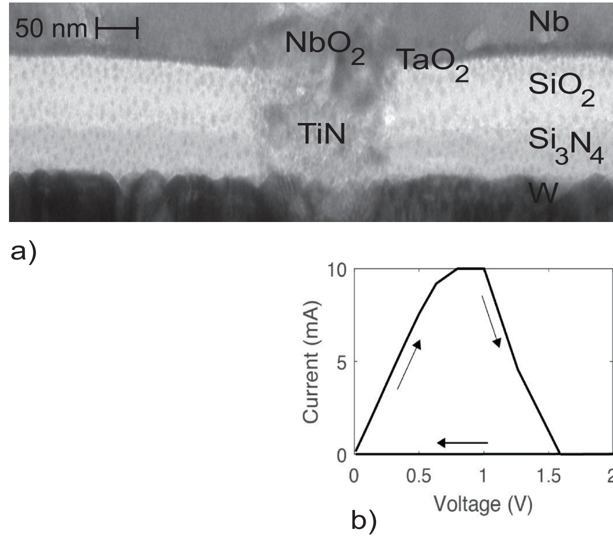

Figure 2.1: Panel a) analytical TEM cross-sectional image of the self-assembled monolithically integrated NbO_2 selector self-aligned to a TaO_2 memristor after electroforming, with approximate locations of material boundaries. The TiN nano-via is 75 nm in diameter and is axially symmetric in the as-fabricated device (i.e. device before the electroforming). The Pt top layer is not shown. Panel b) measured electroforming I-V curves used for model calibration. The authors thank Dr. Kate J. Norris for helpful discussions on electroforming.

transition as the basis of NDR for our selector-memristor structure. Expanding on our computational results, it is suggested the thermodynamical evolution of electroforming is influenced by nano-via geometry, and offers a means of optimizing and tuning selector-memristor behavior and performance. This topic will be the subject of a subsequent publication.

2.2 Self-Consistent Transport Formulation

Self-consistent treatment of coupled transport involving phase change of nanoscale switching material poses a formidable modeling and computational challenge, generally

starting with the Boltzmann equation or molecular dynamics. Electroformation and switching thermodynamics can be modeled, and in fact studied from first principles, by relying on simplifying assumptions that treat transport phenomena as a continuum. Since our focus in this paper is Joule heating occurring in a stack of thin films and its effect on bulk temperature, a reasonable simplification to establish necessary conditions for phase change is the drift-diffusion approximation of thermal and charge transport phenomena. A further simplification can be made assuming there is no circumferential thermal or electric field component to the coupled solution, reducing our 3-D axially symmetric selector-memristor structure of Figure 2.1 to the equivalent planar structure illustrated by Figure 2.2, which also summarizes the composition and dimensions for all the constituent materials.

The drift-diffusion transport approximation reduces to the heat equation and current continuity equations, which in rectangular coordinates for the selector-memristor structure of Figure 2.2 are

$$\rho(\vec{r})C_p(\vec{r})\frac{\partial T(\vec{r},t)}{\partial t} - \nabla \cdot k(\vec{r})\nabla T(\vec{r},t) - Q_f(\vec{r}) = 0 \tag{2.1}$$

$$\nabla \cdot \sigma(\vec{r},V)\nabla V(\vec{r},t) = 0 \tag{2.2}$$

In Equations C.3a and 4.6b, $T(\vec{r},t)$ and $V(\vec{r},t)$ are instantaneous temperature and electric potential, respectively, and $\vec{r}$ is a location in the (x,y) plane of Figure 2.2. Material properties mass density, heat capacity, and thermal conductance are

given by ρ, C_p, and k, respectively. Bulk electrical conductivity of the TaO_2 thin-film exhibits a local temperature dependence of the form $\sigma(\vec{r},T) = \sigma(\vec{r},300) - aT$, where constant a is extracted to provide a continuous linear decrease in electrical conductivty to $\sigma(\vec{r},1200)$[29]. Material parameters for the present study are summarized in Table I[29][30][31][32][33][34][35].

Partial differential equations C.3a and 4.6b are coupled by the Joule heating term, equation C.4, that relates local thermal flux, Q_f, to instantaneous power dissipation due to electronic transport

$$Q_f(\vec{r},V) = \sigma(\vec{r})\left|\nabla V(\vec{r},t)\right|^2 \tag{2.3}$$

A self-consistent general solution of equations C.3a - C.4, on the selector-memristor structure of Figure 2.2, is obtained by the Multiphysics Object-Oriented Simulation Environment (MOOSE) multi-physics FEM solver [36][37]. The equations are discretized by an adaptive finite element method and solved by a Jacobian-free Newton Krylov sub-space approach [36][38]. Neumann boundary conditions for equations C.3a and 4.6b are imposed on the left and right edges of the geometry. On the W bottom electrode are imposed Dirchlet boundary conditions of 300 K and 0 V, respectively. The top Pt electrode is convectively coupled to ambient by a simple gap model, with ambient set at 300 K, and electrical potential imposed as a Dirchlet boundary condition of V_{form}.

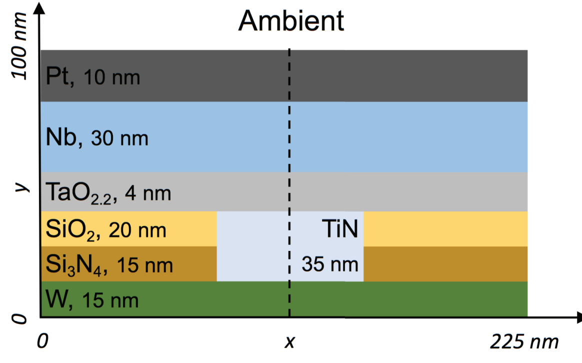

Figure 2.2: Equivalent planar representation of our axially-symmetric memristor-selector structure constructed by assuming there is no circumferential thermal or electric field component to the solution, state prior to electroforming. Ideal electrical and thermal insulating boundaries are assumed on the sides. The bottom W electrode is electrical ground and thermal ambient; the top Pt electrode is convectively coupled to ambient by a simple gap model and the electric potential is V_{form}. The TiN nano-via is 75 nm in diameter. The dashed vertical line centered on the x-axis denotes the cut-section for the temperature and electric potential shown by Figures 2.4 and 2.5

2.3 Simulation and Measurement Results

As the first step to study electrothermal behavior of our devices, a steady-state solution to Equations C.3a - C.4 was found using the MOOSE solver, with the top electrode potential set for V_{form} = 1.3 V, the electroforming bias potential. The steady-state temperature solution is shown by Figure 2.3, illustrating a simulated peak temperature of ≈ 1100 K, in good agreement with our theory explaining IMT of 1081 K of bulk NbO_2 as the basis of NDR in our selector-memristor structure.

Figure 2.4 shows temperature on the cut-section denoted by the dashed line of Figure 2.2, with Figure 2.5 showing electric potential along the same cut-section, for V_{form} = 1.3 V and V_{form} = 0.5 V. These simulation data show that the TiN nano-via couples approximately half the available power from the applied electric field under

Material	$k\left(\frac{W}{m\times kg}\right)$	$\sigma\left(\frac{S}{m}\right)$	$C_p\left(\frac{J}{kg\times K}\right)$	$\rho\left(\frac{kg}{m^3}\right)$
Pt	75	12×10^6	150	40×10^3
Nb	54	40×10^6	270	8.6×10^3
TaO_2	0.10	5×10^2	5.0	8.0×10^3
TiN	20	5×10^6	50	1.1×10^3
W	170	20×10^6	130	19×10^3
SiO_2	1.4	1×10^{-12}	700	2.2×10^3
Si_3N_4	27.0	1×10^{-10}	920	3.2×10^3

Table 2.1: Material and geometry parameters used for simulation.

both bias conditions, although Joule-heating power density is substantially higher in the TaO_2 thin-film, as shown by the peak temperature difference. It is reasonable infer the TiN nano-via plays an influential role in electroforming since its dimensions and material properties establish the heat flux boundary conditions and electric field of our selector-memristor structure, due to their mutual *electrothermal* interaction that is further constrained by the silicon-based insulating thin-films.

To explore this idea further, a transient solution to equations C.3a - C.4 was obtained with the MOOSE solver, with the top electrode similarly set to 1.3 V. Figure 2.6 illustrates the instantaneous temperature located at the top edge of the TaO_2 thin-film and at the geometric center of the TiN nano-via. A thermal time constant can be defined as the time, τ, for instantaneous temperature to increase from 10% to 90%

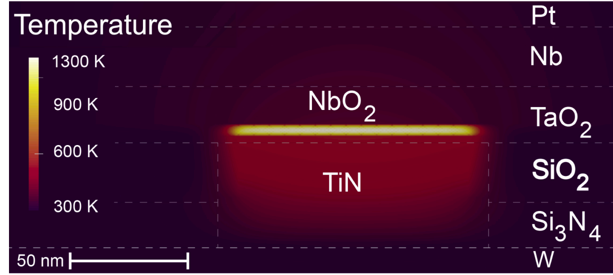

Figure 2.3: Steady-state thermal temperature for $V_{form} = 1.3$ V, illustrating a peak temperature in the thin-film stack of $\approx$ 1100 K and that substantial nano-via self-heating exists. The TiN nano-via is 75 nm diameter and the extent of the material on either side of the nano-via is also 75 nm, for a total width of the geometry of 225 nm. Perfect electrical and thermal insulators are assumed at the sides.The light dashed lines shows the approximate material boundaries; the image is cropped to the right to enhance detail of the selector-memristor structure and nano-via.

of the steady-state temperature at an arbitrary point (x, y) shown by the geometry of Figure 2.2. Simulation results predict thermal time constants of ≈ 400 ns and ≈ 250 ns at the he top edge of the TaO_2 thin-film and at the geometric center of the TiN nano-via, respectively, illustrating varying rates of thermal evolution embedding our selector-memristor structure.

2.4 Discussion

The drift-diffusion formulation for self-consistent electrothermal transport simulation of our selector-memristor structure yields a solution consistent in support of our theory suggesting that thermally activated oxidation of the Nb thin-film by the

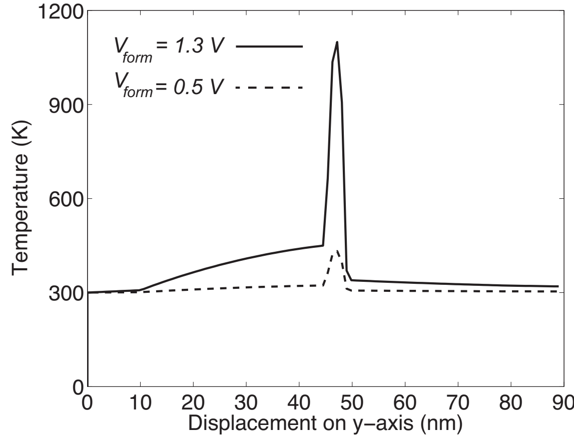

Figure 2.4: Steady state temperature, T, along the cut-section shown by the dashed vertical line in Figure 2.2. Temperature is shown for $V_{form} = 1.3$ V and $V_{form} = 0.5$ V.

TaO_2 yields a self-aligned selector and that insulator-to-metal phase transition of NbO_2 yields NDR. Specifically, at $V_{form} = 1.3$ V the steady-state temperature at the selector-memristor interface was shown to be ≈ 1100 K, indicating conditions favorable for insulator-to-metal transition, which occurs at 1081 K for bulk NbO_2.

Demonstration of electrothermal heating in excess of the NbO_2 IMT temperature supports two important inferences on the thermodynamical evolution of our selector-memristor structure. As noted by Norris, electroforming can produce either NbO_2 or Nb_2O_5 although the electrically conducting phase is preferred due to the negative feedback induced by the larger voltage drop across any local region remaining in the insulator state[24]. Electrodynamic NDR of our selector-memristor simulation is illustrated in Figure 2.6 by the $\approx 10\%$ reduction in the equivalent linearized steady-state temperature, below IMT. This response trends consistently with our theory that locally preferential oxidation of Nb to NbO_2 results in a local decrease in temperarture and

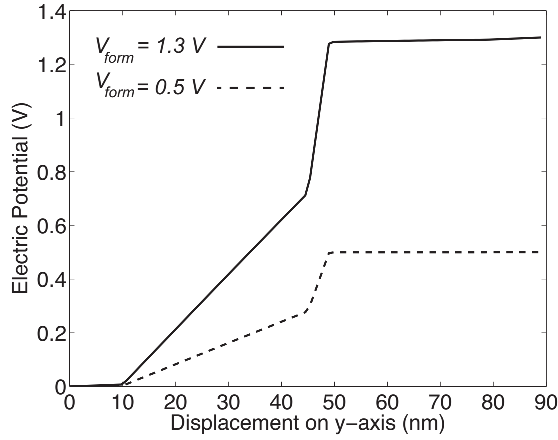

Figure 2.5: Steady-state electric potential, V, along the cut-section shown by the dashed vertical line in Figure 2.2. Electric potential is shown for $V_{form} = 1.3$ V and $V_{form} = 0.5$ V. Note that the available electric field power is coupled in approximately equal proportion to the self-heating of the TaO_2 thin-film and TiN nano-via.

current density in steady-state electroformation, manifested as NDR.

The self-consistent solution illustrated by Figure 2.3 shows that multiple coupled transport phenomena may exist at various stages of the thermodynamical evolution, suggesting an effective method of understanding, controlling, and optimizing electroforming. The TiN nano-via in particualr evidently plays a fundamental role in electroforming thermodynamics, as its dimensions and material properties influence the instantaneous temperature distribution and electric field due to mutual electrothermal interaction between itelf and our selector-memristor structure. Indeed, a key benefit of our drift-diffusion formulation is the ability to discriminate and decouple the mutual interaction of these effects. In this regard, the TiN nano-via acts as a throttle for independent control of thermal flux and current flux due to electric field.

Consider that in steady-state, the power available from the applied electric

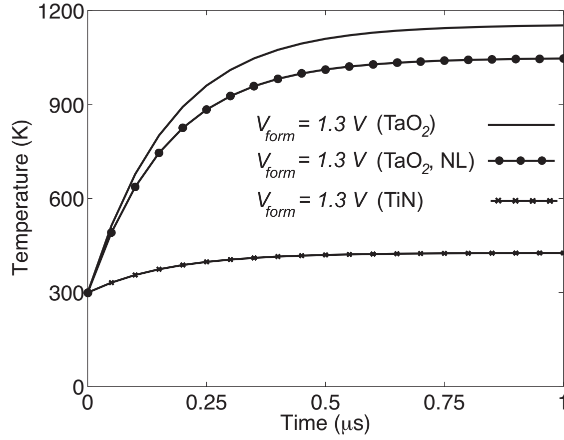

Figure 2.6: Instantaneous temperature T, at the top edge of the TaO_2 thin-film and the geometric center of the TiN nano-via, with $V_{form} = 1.3$ V. Instantaneous temperature of the TaO_2 thin-film is also shown for nonlinear electrical conductivity, illustrating NDR under transient electroformation. This simulation is denoted by NL, and represents the transient solution with electrical conductivity a function of T, described in Section III.

field is coupled to the TaO_2 thin-film and the TiN nano-via in approximately equal proportion, as shown by the potential energy diagram of Figure 2.5. This enables extraction of an equivalent thermal network from the transient results provided by Figure 2.6, yielding the thermal model parameters and equivalent lumped thermal network shown by Figure 2.7. Model parameters are extracted at the top edge of the TaO_2 thin-film and the geometric center of the TiN nano-via, respectively. In this model, volumetric thermal flux, Q_f Equation C.4 is reduced to a point flux at (x, y), and R_{TH} and C_{TH} represent equivalent thermal resistance and heat capacity at (x, y), respectively. Instantaneous temperature, $T(x, y)$ is the equivalent local temperature increase due to the net local flux and heat capacity. Transport model parameters for the simulation were based on the measured data shown in Panel b) of Figure 2.1.

At an electroforming potential of $V_{form} = 1.3$ V, the simulated current is ≈ 10

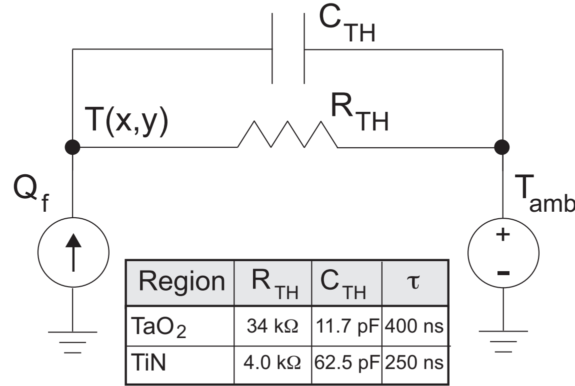

Region	R_{TH}	C_{TH}	τ
TaO_2	34 kΩ	11.7 pF	400 ns
TiN	4.0 kΩ	62.5 pF	250 ns

Figure 2.7: Lumped electrothermal equivalent parameters for thermal transient response model, illustrating substantial inhomogeneity.Note that conventional units for R and C are shown, however strictly speaking, the units are K/W and J/K, respectively.

mA, yielding an approximate equivalent thermal resistance located at the top edge of the TaO_2 thin-film, symmetric on the x-axis, of ≈ 34 kΩ and associated thermal capacitance of 11.7 pF. Similarly, at the geometric center of the TiN nano-via the equivalent thermal resistance is $\approx$ 4.0 kΩ, yielding an associated thermal capacitance of 62.5 pF. This simple model illustrates there is substantial inhomogeneity in the electrothermal evolution of our memristor-selector structure and that a distinguishing feature of the present simulation formulation is identification of these different regimes and the ability to optimize their mutual interaction. Our simulation results are qualitatively consistent with selectors of similar composition and geometry [2].

The ideas presented in this section can be generalized by considering the measured i-v trajectory of panel b) of Figure 2.1. It is evident that local mutual interaction of temperature and electric potential will impact the bulk properties of our selector-memristor structure, with electroforming duration and intensity establishing ultimate steady-state behavior. To generalize this idea, consider current and voltage of Figure

2.1 as arbitrary control parameters in phase space, as shown by Figure 2.8. Here are illustrated two distinct trajectories drawn as a function of an electric field control axis and a charge control axis, defined in arbitrary units. Phases A, B, and C represent three different abstract instantaneous states of electroforming evolution depending duration and intensity. This state-space view of electroforming suggests there are multiple electroforming paths to attain the same terminal performance, perhaps one path that requires little to no electroforming.

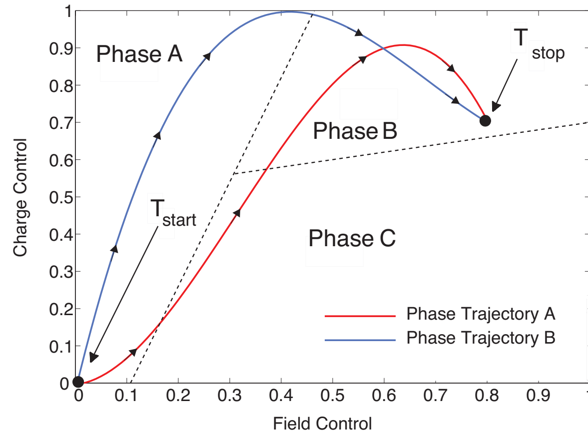

Figure 2.8: Phase space representation of electroforming illustrating two different thermodynamical trajectories. Note that although both trajectories terminate at the same final state, the vastly different paths taken illustrates that different transport and emission phenomena are excited and that their order of excitation will influence the electroformed *i*-*v* characteristics of our selector-memristor structure in particular.

As examples, in Figure 2.8, each trajectory represents two different thermodynamical paths to reach a point in, for instance, Phase B for electroforming. Specifically, the TiN nano-via dimensions will influence thermal and electrical evolution of the selector-memristor structure through mutual electrothermal interaction, and that by throttling thermal flux and current flux, independently, various trajectories can be

traversed, depending on how the stimuli are provided to reach a specific final phase. More importantly, various final phases will be attained depending on a specific trajectory traversed by providing unique combination of the stimuli associated with distinctive structural characteristics of a device.

2.5 Summary

Self-assembled NbO_2 thin-film selectors self-aligned to TaO_2 memristive memory cells have been studied by a multi-physics electrothermal simulation using a drift-diffusion transport approximation. Our steady-state simulation shows conditions in our structure suitable for the formation of thermodynamically stable NbO_2, yielding a self-aligned selector, comparing favorably with our measured results and providing physical insight into electrical and thermal interaction and evolution of the electroforming process [24][6][7].

Our transient simulation shows that the TiN nano-via plays a fundamental role in electroforming, as its dimensions and material properties establish the global temperature distribution and electric field due to mutual electrothermal interaction between our selector-memristor structure and the TiN nano-via. Results further suggest the nano-via in general, through its effect on electroforming, may be used for i-v trajectory and performance optimization.

Chapter 3

Self-Consistent Continuum-Based Transient Simulation of Electroformation of Niobium Oxide-Tantalum Dioxide Selector-Memristor Structures

3.1 Introduction

The study of electroformation of memristive devices is one of the critical issues for both practical and theoretical reasons, particularly for performance optimization, yield enhancement, and reliability improvement [14][7][6][8][39]. Recently it has been suggested that electroformation can be controlled, or designed, to preferentially evolve

to optimize performance, possibly reducing, or eliminating, the need for electroforming [9]. Such a process or device technology might substantially accelerate adoption of memristive-based memory structures and related logic structures, such as neuromorphic cores [22].

Various computational approaches have been applied to explain and optimize memristive behavior. Nardi and Larentis posed a self-consistent [1] electrothermal finite-element formulation coupled to the mass transport equation, demonstrating transport of mobile ionic oxygen can be treated as Frenkel emission [3][4]. Kim illustrated a similar method to that of Nardi [5]. Gibson demonstrated steady-state negative differential resistance (NDR) in niobium oxide selectors using a compact behavioral model self-consistently coupled to a lumped self-heating network [2]. Geist presented a computational formulation of electrothermal transport self-consistently coupled to the mass transport equation, using a simplified filament model [40]. Threshold switching effects of niobium oxide thin-film and memristor structures have also been simulated and studied using various physical approximations based on self-consistent electrothermal transport phenomena [41][42][43][44][45]. While these computational approaches offer wide insight to threshold switching behavior, a general computational approach to electroformation of hybrid niobium oxide-tanatalum dioxide selector-memristor device technology would be of considerable value to compliment the further understanding of their physical behavior and performance optimization [9].

[1] By self-consistent it is meant each of the associated transport equations reach an equilibrium solution in which all equations are solved simultaneously. This is equivalent to multi-physics simulation.

The present computational study was motivated by several key implications obtained by self-consistent continuum electrothermal simulation and experimental characterization of our niobium oxide-tantalum dioxide selector-memristor structures, specifically electroformation [6][7][8][9]. While our continuum electrothermal formulation demonstrates Joule heating produces conditions necessary for oxidation of niobium by tantalum dioxide, and its subsequent insulator-metal transition, to explore transient characteristics of selector electroformation requires a dynamical description of thermally-activated charge transport. With our approach, the insulator-metal transition of niobium oxide from its high-resistance amorphous state to its metallic low-resistance state is treated as a localized continuum change in resistivity, producing a decrease in local Joule heating and initiating a self-limiting effect on spontaneous selector formation. It is the complex thermodynamic evolution of electric potential, temperature, and charge density, and their self-consistent interaction, that establishes ultimate selector behavior. While equivalent lumped-model formulations can replicate hybrid selector-memristor behavior, the continuum formulation naturally admits inhomogeneous mutual interaction, geometry, and interface effects that are central to the transient study of electroforming[2][45].

Electroformation of our niobium oxide-tantalum dioxide selector-memristor structure is studied *ab initio* by augmenting an electrothermal drift-diffusion formulation with Frenkel ionic vacancy transport to model the influence of niobium oxidation and insulator-metal transition. Our formulation does not *a priori* require assumptions regarding conducting filament formation, instead treating electroformation as a con-

tinuum self-consistently satisfying differential conservation laws under non-equilibrium conditions. Transient Type I electroforming simulation of this niobium oxide-tantalum dioxide selector-memristor structures suggests niobium oxide evolution to its stable metallic phase, versus a crystaline Type II insulating phase, produces a localized continuum resistivity decrease, enabling a controlled self-limiting effect on spontaneous electroformation[2][46][47][2]. Our results suggest a new method to finely tailor electroformation processes by explicitly tuning pre-fabrication device design and post-fabrication electrical operations for optimum initial conditioning.

3.2 Formulation of Equations of State

Self-consistent treatment of nano-scale transport phenomena is generally posed as an N-body problem, for example a molecular dynamics (MD) formulation[48][19]. Formulation of niobium oxide-tantalum dioxide selector-memristor electroformation as N-body MD transport treats oxidation, and insulator-metal transition, as mutual interaction and displacement of individual charge carrier and vacancies. However, if it is unnecessary to understand the displacement of individual charge carriers, a continuum formulation replaces the equation of motion posed by MD with a charge density subject to conservation laws that are also satisfied by the MD equations of motion, considerably simplifying the formulation. Our approach replaces the Langrangian reference-frame of MD with a Eulerian reference-frame that is fixed in space but nevertheless dynamically

[2]Refer to the Supplemental material of Gibson for further details on Type I and Type II electroforming.[2]

emulates advection and diffusion of thermally-activated charge densities and vacancies and their self-consistent interaction with electric potential and local temperature.

Electroformation and threshold switching behavior can be modeled, and in fact studied from first principles, by relying on simplifying assumptions that treat transport phenomena as a continuum [6][7][8][39]. In the continuum formulation, dynamical evolution is appropriately described by the Boltzmann transport equation, and its various moments, such as drift-diffusion [49]. Previously, to study the transient response of our niobium oxide selector, self-aligned to a tantalum dioxide memristor, state equations were obtained by posing a self-consistent drift-diffusion formulation of electrothermal transport coupled to a phenomenological conductivity model [9]. This formulation yields the heat equation and current continuity equations, which in rectangular coordinates for our selector-memristor structure are

$$\frac{\partial T(\vec{r},t)}{\partial t} = S_T(\vec{r}) + S_J(\vec{r}) \tag{3.1}$$

$$\nabla \cdot \sigma(\vec{r},T)\nabla V(\vec{r},t) = 0 \tag{3.2}$$

where $\vec{r}$ is a location the (x, y)-plane of the planar cross-section of our axially-symmetric structure, and $T(\vec{r},t)$ and $V(\vec{r},t)$ are local temperature and electric potential state variables, respectively.

Material layer description and dimensions of our selector-memristor structure are given in Table I. The as-fabricated device used for the present study comprises a bottom W electrode followed by a TiN via surrounded by a bilayer structure of Si_3N_4

and SiO_2. The TiN via is followed by planar $TaO_{2.2}$ and Nb layers, and further followed by a Pt top electrode[9].

Material	Thickness (nm)	Width (nm)
Pt	10	225
Nb	30	225
$TaO_{2.2}$	4.0	225
TiN	35	75
W	15	225
SiO_2	20	75
Si_3N_4	15	75

Table 3.1: Material description, layer thickness, and width of equivalent planar representation of our axially-symmetric memristor-selector structure constructed by assuming zero circumferential thermal or electric field component. Specific details of the 2-D equivalent selector-memristor structure were previously published.

The right-hand side of Equation C.3a represents diffusive thermal transport, $S_T(\vec{r},t)$, and Joule heating, $S_J(\vec{r},t)$, respectively, as source terms

$$S_T(\vec{r},t) = \nabla \cdot \kappa(\vec{r}) \nabla T(\vec{r},t) \tag{3.3}$$

$$S_J(\vec{r},t) = \left[\frac{\kappa(\vec{r})}{k_{th}(\vec{r})} \right] \sigma(\vec{r},T) \left| \nabla V(\vec{r},t) \right|^2 \tag{3.4}$$

with thermal diffusivity and thermal conductivity defined as $\kappa(\vec{r}) = \frac{1}{\rho c_p} k_{th}(\vec{r})$ and $k_{th}(\vec{r}) = \sigma(\vec{r},T) \times T(\vec{r},t)$, where ρ and c_p are mass density and specific heat, respectively. Thermal conductivity is assumed to obey the Wiedemann-Franz law, with

the Lorenz number being expressed as a function of temperature in the range of interest, and $\sigma(\vec{r}, T)$ a phenomenological conductivity model[3][4][5].

It is evident a phenomenological conductivity [3] model obscures fundamental physical behavior, particularly the influence of thermally activated charged particles, such as ionic oxygen vacancies, on the dynamical evolution of niobium oxidation and electroformation. Experimental analysis of electroformation on our selector-memristor structure suggests reduction of $TaO_{2.2}$ by Joule heating produces oxygen vacancies [6][7][8]. In the continuum approximation, thermodynamical evolution of this reduction can be represented by the addition of oxygen vacancy density, $n(\vec{r}, t)$, as an additional state variable, with instantaneous conductivity expressed now as

$$\sigma(\vec{r}, n, T) = n(\vec{r}, t) \times \mu(\vec{r}, T) \times q \tag{3.5}$$

where $\mu(\vec{r}, T)$ is an associated mobility function and q is electron charge. Ionic oxygen vacancy transport in the Eulerian continuum formulation can be approximated as Frenkel emission

$$S_F(\vec{r}, t) = \nabla \cdot D_F(\vec{r}, \vec{x}) \nabla n(\vec{r}, t) - [\nabla \cdot v_F(\vec{r}, \vec{x})]\, n(\vec{r}, t) \tag{3.6}$$

[3]In contrast to a quasi-static phenomenological conductivity model, the dynamic influence of electroformation on instantaneous conducctivity is formulated by considering the thermal activation of mobile electrical charges and their self-consistent electrothermal advection and diffusion with electric and thermal fields dynamically established within the device, subject to Frenkel defect transport. This formulation enables the true physical nature of negative differential resistance, insulator-metal transition, and electroformation to be dynamically studied.

where Frenkel diffusion and drift velocity are given by

$$D_F(\vec{r}) = D_o exp(-\beta E_{ac}^D) \tag{3.7a}$$

$$v_F(\vec{r}, \vec{x}) = \mu_F(\vec{r}, \vec{x}) \times \nabla V(\vec{r}, t) \tag{3.7b}$$

Drift velocity is related to electric potential by Frenkel mobility

$$\mu_F(\vec{r}) = \frac{1}{T} exp(-\beta E_{ac}^{\mu}) \tag{3.8}$$

where E_{ac}^D and E_{ac}^{μ} are activation energies for diffusion and drift, respectively [3][4][5][2][49][50][51].

Instantaneous Frenkel emission contribution to conductivity, to approximate insulator-metal transition to the metallic low-resistance state, is self-consistently coupled to equations of state C.3a and 4.6b by the mass transport equation

$$\frac{\partial n(\vec{r}, t)}{\partial t} = S_F(\vec{r}) + \sum_{k=1}^{K} S_k(\vec{r}, t) \tag{3.9}$$

where $S_k(\vec{r}, t)$ represents additional emission terms, specifically thermally-activated production of ionic oxygen vacancies by the $TaO_{2.2}$ layer. Electronic transport for the metallic and silicon-based thin-film layers and the TiN nano-via was approximated by a Drude relaxation-time model[49].

3.3 Discussion

To study the transient evolution of electroformation of our niobium oxide-tantalum dioxide selector-memristor structure *ab initio*, a self-consistent solution of state equations C.3a, 4.6b, and 4.5 is obtained by the Multiphysics Object-Oriented Simulation Environment (MOOSE) finite-element platform [36]. The equations of state are discretized by an adaptive mesh algorithm and solved by a Jacobian-free Newton Krylov sub-space method. Zero-flux electric potential, temperature, and charge Neumann boundary conditions are imposed on the left and right edges of the discretized selector-memristor structure [38][37]. On the bottom W contact are imposed Dirichlet boundary conditions of temperature 300 K and electric potential 0 V, respectively. The top Pt contact is convectively coupled to 300 K ambient by a simple gap model, with V_{form} imposed as a Dirichlet boundary condition on electric potential [36].

Figure 3.1 illustrates the equivalent discretized selector-memristor structure used in the current computational study. To simplify the analysis, it is assumed niobium oxidation and insulator-metal transition takes place within 5 nm above the initial niobium-tantalum dioxide interface; it is this region that is constrained to exhibit oxidation, insulator-metal transition, and electroformation, by self-consistently satisfying differential conservation laws C.3a, 4.6b, and 4.5. The off-stoichiometric oxygen-rich $TaO_{2.2}$ layer behaves as a charge reservoir, with an initial condition of 10^{17} carriers per cubic centimeter [3][4][5].

Under the influence of Joule heating, mobile ionic oxygen produced by the

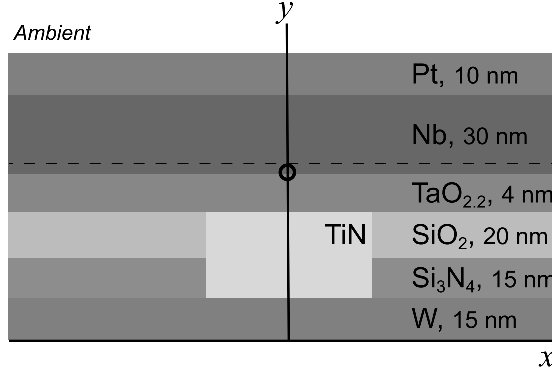

Figure 3.1: Equivalent planar representation of our axially-symmetric memristor-selector structure. The bottom W electrode is electrical ground and thermal ambient; the top Pt electrode is convectively coupled to ambient by a simple gap model and the electric potential is V_{form}. The sides are ideal electrical and thermal insulators. The circle indicates the physical coordinates for $\vec{r}$ for the evaluation of $T(\vec{r}, t)$ and $n(\vec{r}, t)$, local temperature and carrier density respectively. Chemical composition and thickness of each layer are shown. The diameter of the TiN nano-via is 75 nm. The dashed line immediately above the $TaO_{2.2}$ layer represents extent of the region discretized to undergo oxidation.

off-stoichiometric oxygen-rich $TaO_{2.2}$ layer subsequently oxidizes and electroforms the as-deposited niobium layer to its thermodynamically stable metallic phase as $\mathrm{Nb} + 2\,\mathrm{Nb_2O_5} \longrightarrow 5\,\mathrm{NbOx}$ [6][7][8][39]. This electrochemical process precedes an instantaneous decrease of the electric potential across the oxidized niobium selector, due to an irreversible transition from its high-resistance amorphous state (HR) to its metallic low-resistance state (LR), producing a decrease in local Joule heating. This phenomena can be explored by a transient solution of the equations of state described above, which has never been examined in previous studies[9][3][4][2][40].

For the purpose of the current computational study, the electroformation process considered exhibits a distinct and irreversible transition from the virgin HR amorphous state to a final metallic LR state. The current as-fabricated selector-memristor

structure that undergoes electroformation should not be described by referring to turn-off and turn-on, as two states imply the presence of cyclic characteristics. Electroformation is thus defined as an irreversible and non-cyclic process that exhibits an abrupt change in terminal resistivity, and current, at a magnitude much higher than that seen in the cyclic operation.

Figure 3.2 illustrates the transient response of instantaneous resistivity following application of $V_{form} = 1.3$ V at $t = 0$ s, with resistivity defined as the ratio of voltage to current at the top Pt contact of our selector-memristor structure. Resistivity is normalized to the HR amorphous state at $t = 0$ s. It is evident that the ratio of the HR amorphous state resistance to the LR metallic state resistance is greater than 20 dB, indicating formation of a continuum conducting region occurs in ≈ 1 ns transient duration. Note that the present model makes no *a priori* assumptions on conducting region nucleation or morphology, instead treating incipient insulator-metal transition of our niobium oxide selector as a continuum gradient of local resistivity due to advection and diffusion of thermally activated ionic oxygen vacancies self-consistently interacting with electric potential and local Joule heating.

Since no substantial change in resistivity is observed for $V_{form} < 1.3$ V, negative differential resistance is not exhibited by the niobium oxide, and it remains unformed for these lower electric potentials. In the absence of the negative differential resistance introduced by the insulator-metal transition of niobium oxide, our selector structure behaves as a distributed linear Joule-heating network with thermal intertia, largely introduced by the TiN nano-via[9]. A key implication of this electrothermal interac-

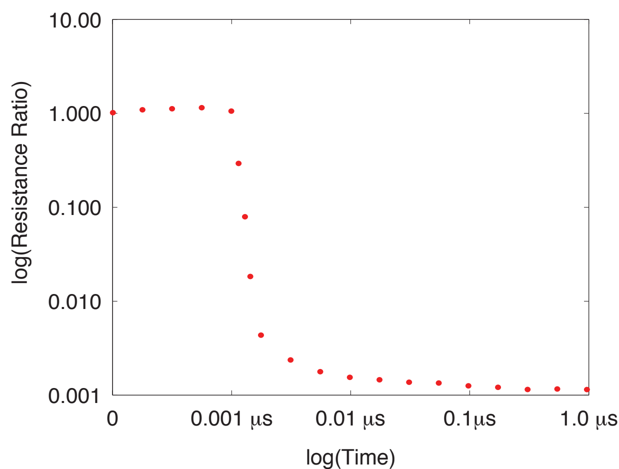

Figure 3.2: Transient response of instantaneous normalized resistivity following application of $V_{form} = 1.3$ V at $t = 0$ s. Resistance is normalized by the HR amorphous resistive state at $t = 0$ s. Creation of a continuum conducting region at the insulator-metal transition temperature of niobium oxide is illustrated by a ratio of the HR amorphous state resistance to the LR metallic state resistance greater than 20 dB.

tion with vacancy transport is formation of a Stefan-type dynamic thermal boundary condition at the niobium oxide-tantalum dioxide interface[52].

Figure 3.2 illustrates the instantaneous temperature field for each of the V_{form} tabulated in Table II; the table also shows for each V_{form} the respective maximum temperature, rise time, steady-state temperature, and time achieve steady-state. Comparing the instantaneous temperature field for $V_{form} = 1.3$ V at $t = 0.95$ ns and $V_{form} = 1.0$ V at $t = 50$ ns it is evident that an insulator-metal transition of the niobium oxide occurs at approximately the insulator-metal transition temperature of 1080 K for the first bias condition but not the second. Similarly, for $V_{form} = 0.5$ V at $t = 50$ ns, there is no insulator-metal transition of the niobium oxide, and electroforming does not occur. Note that the transient event of Joule heating to induce insulator-metal transition

produces negligible initial self-heating of the TiN nano-via. The introduction of negative differential resistance by the niobium oxide during electroforming of our selector substantially reduces the instantaneous power dedicated to heating the niobium oxide, with the remaining electroforming energy lost to heat, serving no further useful purpose.

To develop this idea further, consider Figure 3.4 illustrating the transient response of instantaneous temperature at the geometric center of the niobium oxide thin-film layer for three distinct electric potentials. For a electric potential $V_{form} = 1.3$ V, at approximately 1 ns, following oxidation of the niobium thin-film, it evident an insulator-metal transition occurs and electroforming results. The niobium oxide phase transition to the metallic LR state yields a substantial decrease in Joule heating, subsequently yielding a local decrease in temperature of the formed niobium oxide selector, manifested as negative differential resistance. During this thermodynamical transient, a continuum conducting region is created that establishes the terminal I-V characteristics of our selector structure self-aligned to a tantalum dioxide memristor. For $V_{form} = 1.0$ V and $V_{form} = 0.5$ V it is evident that there is insufficient Joule heating of the niobium thin-film for insulator-metal transition, hence the transient response is free from negative temperature gradient associated with negative differential resistance and electroforming.

Figure 3.4 further illustrates in steady-state, in the absence of a specific external current limit, that substantial Joule heating exists around our niobium oxide-tantalum dioxide selector-memristor structure. The dominant thermal time constant, *i.e.* t_{rise} of Table II, of this distributed Joule-heating network is approximately an

order of magnitude larger than insulator-metal transition of niobium oxide, due to the thermal inertia of the TiN nano-via. The heat flux produced by this Joule heating contributes in a controlled manner to creation of a dynamic interface condition at the niobium oxide-tantalum dioxide interface.

These results suggest possible mechanisms of performance enhancement include selection of physical and material properties favorable to an arbitrarily optimal thermodynamic evolution of our niobium oxide-tantalum dioxide selector-memristor structure. Moreover, since substantial energy is lost to unnecessary heating of the TiN nano-via subsequent to electroformation, restricting the total available energy for electorformation, through external means, simplifies the electroformation process and could lead to improvement in yield and consistency over the selector-memristor array. This approach may be referred to energy-limited, in contrast to power-limited, electroforming. Energy-limited electroforming delivers energy sufficient only to achieve insulator-metal transformation and creation of a conducting region, whereas power-limited electroformation continues to evolve to a distinct equilibrium, established largely by the electrothermal properties of the TiN nano-via.

Figure 3.5 distinguishes Type I and Type II electroforming in phase-space, where initial conditions, material composition, and structure of a niobium oxide-tantalum dioxide selector-memristor coupled with stimulus determine the path taken in phase-space and the ultimate stationary-state representing formed behavior[2][46][47]. In our model, the path taken by Type I electroforming through the insulator-metal transition, due to Joule heating, increases the local concentration of free carriers to approximate a

V_{form} (V)	T_{max} (K)	t_{rise} (ns)	T_{steady} (K)	t_{steady} (ns)
1.3	1049	0.95	570	9.8
1.0	937	8.5	937	50
0.5	478	9.0	478	50

Table 3.2: Transient response comparison for various V_{form}. Maximum temperature, T_{max}, is defined as peak temperature at the geometric center of the niobium oxide thin-film layer. Rise time, t_{rise} is defined as the time from 10% to 90% of the steady-state value. Steady-state conditions, t_{steady} and T_{steady}, , are defined as within 1% of the final value, as determined by the MOOSE solver.

stable metallic low-resistance state of the formed niobium oxide. In contrast, the path taken by Type II electroforming produces a stable crystaline insulating state.

While previous research has suggested various approaches to eliminating or controlling electroformation of memristor structures, we believe that our distinction between energy-limited and power-limited electroformation represents a new interpretation of electoformation. For example, Yang suggested memristor electroforming problems can be largely eliminated by engineering the device structure to remove bulk oxide effects in favor of interface-controlled electronic switching [53]. Recently, Kumar has suggested electroformation exhibited by niobium oxide memristor structures is due to both a current-controlled and a temperature-controlled NDR, due to relatively low-temperature nonlinear transport mechanism and a high-temperature Mott transition, respectively.[54]. Further research is needed for optimal stimulus synthesis of the appropriate composition to excite energy-limited modes to test the current theory for our niobium oxide-tantalum dioxide selector-memristor structure.

3.4 Summary

A self-consistent computational continuum transport formulation of dynamic electroformation that does not make *a priori* assumptions on conducting filament formation has been presented of our self-aligned niobium oxide-tantalum dioxide selector-memristor structure. The transient electroforming simulation results suggests niobium oxide evolution to its stable metallic phase initiates a resistance collapse phenomena, producing a self-limiting effect on spontaneous formation of our niobium oxide selector.

Our computational framework self-consistently treats transient evolution of niobium oxide-tantalum dioxide selector-memristor Type I electroforming, versus steady-state, identifying existence of modes of vastly different time constants operating interactively as a result of specific procedures and conditions established by the act of electroforming. It is evident electroforming stimuli excites distinct dynamical modes whose mutual interaction and behavior establish final niobium oxide-tantalum dioxide selector-memristor behavior. The ultimate response to these modes is also established by initial selector-memristor dimensions and material composition, suggesting the presence of a route to finely tailor electroformation processes by explicitly tuning pre-fabrication device design and post-fabrication electrical operations for optimum initial conditioning of selector structures.

From our computational results, the notion of energy-limited electroforming was introduced, in contrast with power-limited electoforming. Since substantial energy is lost to waste heat during the forming process, providing the energy only necessary to

induce insulator-metal transition may offer a means to optimize selector-memristor performance. Our study clearly suggests that the formation and presence of a conduction channel, or plurality of such channels, is not necessary for the electroformation of our niobium oxide-tantalum dioxide selector-memristor structure. In particular, when the device structure constrains the spatial current distribution, as the TiN nano-via does of our design, local heating at the level required for electroformation is achieved in a controlled and repeatable manner.

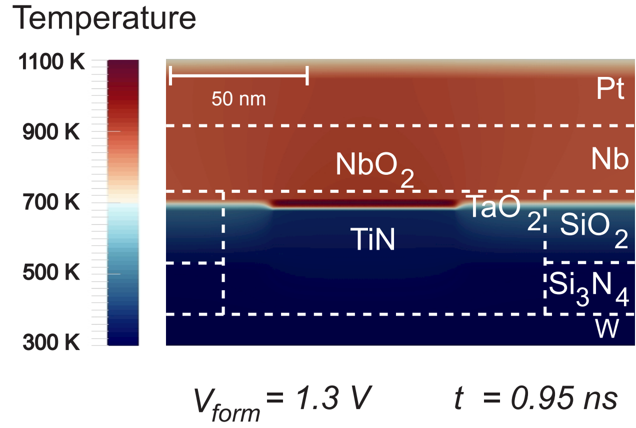

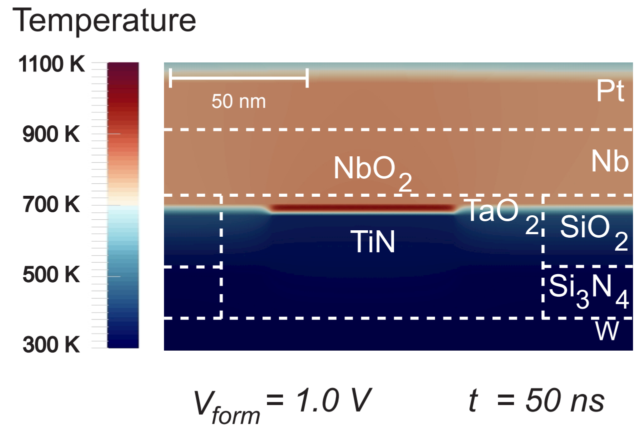

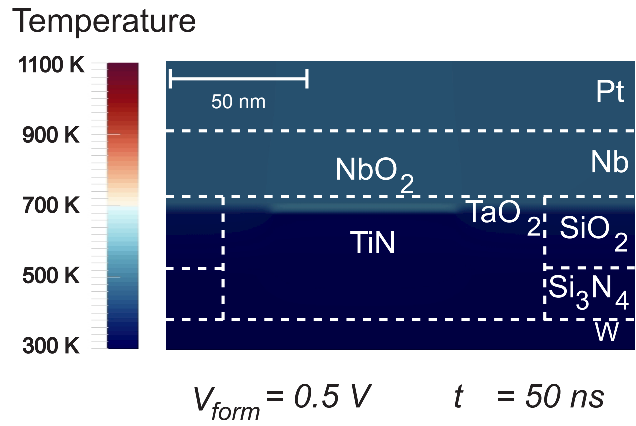

Figure 3.3: Instantaneous temperature 0.95 ns following application of $V_{form} = 1.3$ V at $t = 0$ s; instantaneous temperature 50 ns following application of $V_{form} = 1.0$ V at $t = 0$ s; instantaneous temperature 50 ns following application of $V_{form} = 0.5$ V at $t = 0$ s.

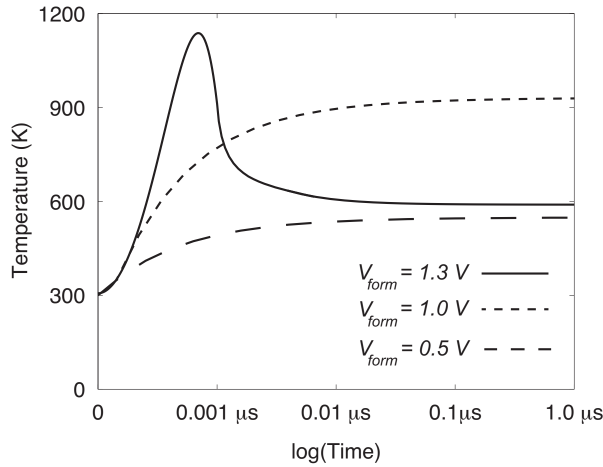

Figure 3.4: Transient response of instantaneous temperature at the geometric center of the niobium oxide thin-film layer, following application of V_{form} = 1.3 V at $t = 0$ s. Instantaneous temperature is also shown for V_{form} = 1.0 V applied at $t = 0$ s and V_{form} = 0.5 V applied at $t = 0$ s. Note that electroforming and negative differential resistance obtain only for V_{form} = 1.3 V. Refer to Table II for a summary of transient response versus electric potential.

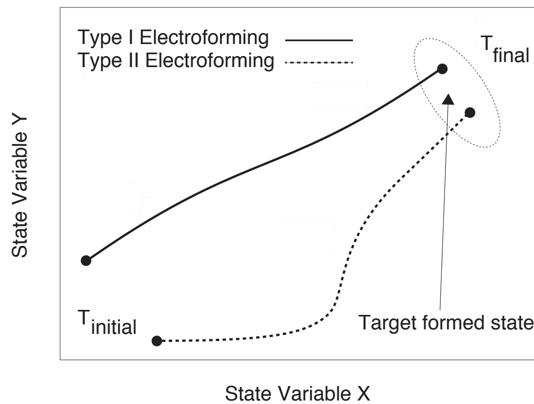

Figure 3.5: Phase-space dynamical evolution of Type I and Type II electroforming, with only two state variables shown, which could be, for example, applied electric potential and temperature at a geometric location in the (x, y)-plane of Figure 3.1.The idea represented by the diagram is that various trajectories of dynamical evolution are possible, depending on initial conditions, material composition and structure of a niobium oxide-tantalum dioxide selector-memristor. The final formed state, at T_{final}, occurs in a region of phase-space where desired performance obtains. In following with the phase-space diagram previously presented, it is important to note that various configurational and thermodynamic phases may be encountered by a specific trajectory.

Chapter 4

A Computational Phase-Field Study of Possible Mechanisms of Conducting Channel Formation in Dielectric Thin Films

4.1 Introduction

Physical and chemical properties of dielectric thin films for resistive switching are governed by the dynamical behavior of intrinsic atomic metastable states of thin film materials and the presence of irreversible states endowed by specific preparation processes. Atomic metastable states may arise from various phenomena, such as Mott localization or change in configurational entropy, producing such effects as insulator-metal transition and hysteresis often seen in appropriately prepared dielectric

thin films[55],[56],[57],[58]. When two chemically distinct and spatially distinct materials separated by an interface are forced to interact, they would, in the steady-state, produce either a uniform solid solution or decompose into two distinct phases via phase separation, depending on their mutual affinity associated with their unique bulk free-energy density. However, the morphological evolution of the interface separating each material is inherently dynamic and naturally produces complex microstructure resulting from various interactions of bulk free-energy, interface energy, electrothermal phenomena, and electrochemical phenomena the interface experiences[59]. Therefore, distinctive microstructure is expected to appear at the interface to self-consistently minimize the total energy, which in turn result in characteristic transport properties fundamental to, for instance, resistive switching behavior exhibited by dielectric thin films[58],[60].

Various qualitative models have been adopted to study resistive switching behavior of dielectric thin films, largely based on formation of conducting channels composed of clusters of charged species[10],[11],[12],[13]. These models invoke both electronic transport and ionic transport, often treated as electrothermal and electrochemical processes, respectively, reproducing both unipolar and bipolar resistive switching behavior. This conducting channel formalism suggests an initial irreversible growth of cluster-like aggregates composed of charged species forming conducting channels, as illustrated by Figure 4.1. These conducting channels subsequently form and rupture under the influence of an external electric potential, yielding resistive switching behavior.

Numerous computational studies have adopted the conducting channel for-

malism to advance theories on resistive switching that occurs in thin films made of dielectric materials. Xu posed a qualitative conducting channel model based on experimental data suggesting clustering and bifurcation of thread-like conducting channels to explain set and reset processes of bipolar resistive RAM (RRAM) devices[10]. Pan presented a similar study, with empirical evidence supporting formation and rupture of conducting channels corresponding to low-resistance and high-resistance states, respectively, of their ZnO memristor[11]. Ielmini presented a self-consistent electrothermal computational study based on a thermally activated ion migration model demonstrating conducting channel formation and rupture [12]. Using an analytical formulation, the approach correctly resolved set and reset behavior of a generic bipolar RRAM device by dynamic coupling of the channel resistance, charge transport and temperature, providing insight on conducting channel dynamic behavior. Gibson demonstrated steady-state negative differential resistance in niobium oxide selectors using a compact behavioral model self-consistently coupled to an electrothermal network. Their model demonstrated insulator-metal transition is not required for the presence of negative differential resistance, being due instead to Frenkel transport[2]. In contrast, Sevic posed a continuum-based computational study of the dynamical evolution of niobium oxide selector electroforming[8],[9].

The conducting channel formalism has been complimented by several empirical studies on channel morphology and effect on transport properties of mobile charge carriers as the mechanism fundamental to resistive switching behavior. Yang and Strachan, in two complimentary studies of titanium oxide thin films using atomic force

microscopy and transmission electron microscopy, provided experimental evidence of regions of dynamic conductivity modulation corresponding to set and reset. Their studies also indicated resistive switching behavior of their structure is related to a localized partial reduction of titanium dioxide and subsequent formation of a metallic conducting channel[53],[61]. Miao studied tantalum oxide thin films using pressure-modulated conductance microscopy to identify regions of dynamic conductivity modulation. Transmission electron cross-sectioning of these modulated regions suggested presence of conductive channels[62]. Ahmed used electron energy loss spectroscopy to observe formation and rupture of the oxygen deficient conducting channels goverening charge transport phenomema in their perovskite strontium titanate metal-insulator-metal (MIM) structure[13]. Their results suggest the presence of complex interface microstructure and spinodal decomposition distinguishing the semi-metallic conducting channels embedded in amorphous bulk.

While the conducting channel formalism qualitatively explains resistive switching behavior of dielectric thin films, in contrast, previous computational studies have largely adopted a continuum transport formulation. Self-consistent solution of the continuum transport equations dynamically emulates advection and diffusion of thermally-activated charged species, and their interaction with local electric potential and temperature, to model bulk resistive switching phenomena. The continuum formulation, however, depends vitally on an *a priori* conducting channel transport model and correct identification of diffusion and mobility expressions for each specific transport mechanism, for example Frenkel transport for ionic vacancy conduction[2],[9],[8],[3],[4],[5],[14],[15].

A computational formulation that does not *a priori* impose assumptions on conducting channel morphology, transport phenomena, or interface uniformity, and instead treats resistive switching from its origin at the atomic-scale, may offer significant advantages over existing methods. Such a method might model the dynamical evolution of cluster-like charged aggregates, as illustrated by Figure 4.1, subject to their atomic and interfacial electrothermal interaction, naturally producing conducting channels in a non-conducting host. The phase field method is one such method[16],[17],[18],[19].

In this paper, we apply a phase field method to study dynamical evolution of conducting channels that influence resistive switching behavior exhibited by dielectric thin films. With the phase field method, the assumptions of an *a priori* conducting channel model and the presence of specific transport phenomena to explain resistive switching are abandoned, and our model is instead formulated as a diffuse interface problem subject to a variational principle[20]. Our approach successfully predicts the formation of conducting channels in typical dielectric thin film structures comparable to a range of resistive switches, offering an alternative computational formulation based on metastable states treated at the atomic scale, requiring no assumptions on conducting channel morphology and its fundamental transport mechanisms. Further, our approach applies to both electronic transport and ionic transport, *e.g.* ionic oxygen vacancies, however the current study focuses exclusively on electronic transport of dielectric thin films and unipolar resistive switching.

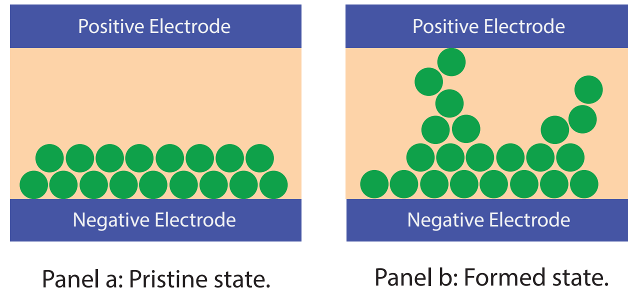

Figure 4.1: The conducting channel formalism illustrated by a charged species cluster model. Panel (a) illustrates the pristine pre-formed state; panel (b) illustrates a possible formed state, showing one complete conducting channel forming a continuous path between the negative and positive contacts. The green circles represent discrete charged species, hosted by a dielectric, shown in tan. The phase field formulation tracks the dynamical evolution of the envelope of clusters of these charged species, whose interface collectively constitutes a conductive channel, subject to a variational principle and local conservation laws.

4.2 Self-Consistent Phase-Field Formulation

Charge transport properties of thin films, governed by the dynamical behavior of atomic metastable states, are naturally treated by the phase field method. In contrast to molecular dynamics, which tracks the motion of each charge carrier, the phase field formulation tracks the dynamical evolution of the envelope of clusters of charge carriers whose aggregate boundary, an *a priori* unknown, forms a conducting channel interface within the non-conducting host, as illustrated by Figure 4.1. The phase field formulation thus avoids the mathematically onerous problem of expressing dynamic boundary conditions over an interface whose location is part of the unknown solution. In our study, self-consistent solution of the phase field equation yields the dynamical evolution of the interface formed between the conducting state and non-conducting state, both of

which co-exist in a dielectric thin film, subject to local conservation laws.

To apply the phase field formulation, consider Figure 4.2 illustrating a pristine dielectric thin film structure composed of a conducting region and a non-conducting region, separated by an interface represented by the dotted horizontal line. This initial structure is viewed as an as-fabricated resistive switch comprising a dielectric thin film in which two distinct regions are separated by an interface, comprising a resistive switch made of a dielectric thin film in which mobile charges are initially distributed in a certain way creating the two regions, one conducting and the other non-conducting. This specific initial structure allows a double-well free-energy density function and the diffuse interface approximation to suitably describe dynamical structural evolution within our dielectric thin films. The bulk free-energy density function associated with the dielectric thin film structure of Figure 4.2 is given by

$$f_{bulk}(c) = A \times \Big[c(\vec{r},t) - c_1\Big]^2 \Big[c(\vec{r},t) - c_2\Big]^2 \tag{4.1}$$

where A is the magnitude of the double-well potential, c_1 and c_2 represent normalized concentration of the conducting and non-conducting states, respectively, and $c(\vec{r},t)$ is the concentration variable, an unknown[1]. The concentration is bounded to the interval $0 \leq c(\vec{r},t) \leq 1$, with unity corresponding to the pure conducting state and zero corresponding to the pure non-conducting state. Here $\vec{r}$ represents a location in the (x, y)-plane of the structure of Figure 4.2 and t is time.

Interaction of the bulk free-energy and interface energy with electric potential

[1] The normalization constant has been suppressed.

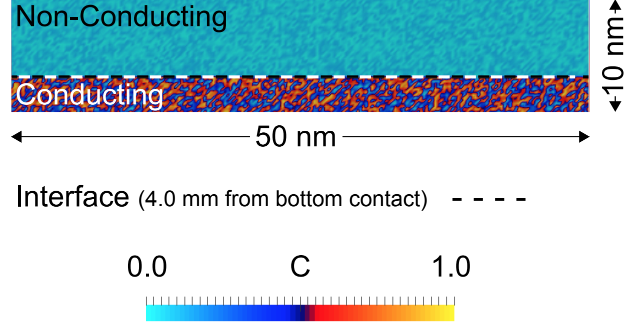

Figure 4.2: A pristine dielectric thin film structure composed of a conducting region and a non-conducting region to approximate an as-fabricated resistive switching device. The interface is represented by the dotted horizontal line, and is 4 nm from the bottom edge. The pristine concentration is established by an initial concentration, $c(\vec{r}, 0)$, uniformly distributed between 0.1 and 0.3 for the non-conducting state and 0.7 and 0.9 for the conducting state. The structure is 50 nm × 10 nm.

externally applied to the structure of Figure 4.2 is modeled by the following electrostatic energy term

$$g_{elec}(c, V) = \frac{q}{\Omega} V(\vec{r}, t) c(\vec{r}, t) \tag{4.2}$$

where $V(\vec{r}, t)$ is electric potential between the top and bottom edges of the structure, q is electronic charge, and Ω is a differential volume unit[2]. The free-energy functional obtains by combining Equations 4.1 and 4.2 with an interface gradient energy term to yield

$$F = \int_R \left[f_{bulk}(c) + \frac{\kappa}{2} \nabla^2 c(\vec{r}, t) + g_{elec}(c, V) \right] d\vec{r} \tag{4.3}$$

where κ is an interfacial gradient energy term that relates to energy stored per

[2]For the current formulation, Ω is the volume of a mesh cell, of unit depth, following finite-element discretization of the structure of Figure 4.2.

unit application of the potential of the gradient of $c(\vec{r},t)$ and the integration is over R, entire thin film structure of Figure 4.2. Interfacial gradient energy is assumed to be uniformly constant along the interface.

The phase field transport equation is found by seeking an energy-minimizing stationary state of the free-energy, identified by finding the first-order variation of free-energy functional Equation 4.3. From the first-order variation of free-energy functional Equation 4.3, the phase field flux obtains

$$J_{PF} = M\nabla\left[\frac{\partial f_{bulk}(c)}{\partial c} - \boldsymbol{\nabla}\cdot\kappa\nabla c(\vec{r},t) - \frac{q}{\Omega}V(\vec{r},t)\right] \tag{4.4}$$

where M is an associated mobility of the phase field flux in phase-space, and assumed constant. Since the concentration variable, $c(\vec{r},t)$, is conserved, the phase field conservation law obtains

$$\frac{\partial c(\vec{r},t)}{\partial t} = \boldsymbol{\nabla}\cdot J_{PF} \tag{4.5}$$

This is the Cahn-Hilliard phase field equation in concentration variable $c(\vec{r},t)$ for our dielectric thin film model[63]. The dynamical evolution of the conducting channel, created at the interface formed by the conducting and non-conducting states, under the influence of an externally applied electric potential, is described by phase field conservation Equation 4.5 self-consistently coupled to the electronic Laplace equation

[9],[20]. This yields

$$\frac{\partial c(\vec{r},t)}{\partial t} = \boldsymbol{\nabla} \cdot M\nabla\left[\frac{\partial f_{bulk}(c)}{\partial c} - \boldsymbol{\nabla} \cdot \kappa\nabla c - \frac{q}{\Omega}V\right] \tag{4.6a}$$

$$\nabla \cdot \sigma\left[c(\vec{r},t)\right]\nabla V(\vec{r},t) = 0 \tag{4.6b}$$

where local conductivity, $\sigma\left[c(\vec{r},t)\right]$, is a linear positive-monotonic function of concentration, $c(\vec{r},t)$[3]. For the current computational study, an isothermal assumption is made for the initial forming process. Our current focus is to assess the applicability of the phase field method in the context of conducting channel formation in dielectric thin films, although we are fully aware of the importance of thermal effects used in our study and their intrinsic influence on the outcome[8],[9].

To study the dynamical evolution of conducting channel formation of our thin film structure, a self-consistent solution of Equation 4.6a and Equation 4.6b is obtained by the Multiphysics Object-Oriented Simulation Environment (MOOSE) finite-element platform [36],[38],[37],[64]. Periodic boundary conditions are imposed on the left and right edges of the discretized thin film structure of Figure 4.2 for both electric potential, $V(\vec{r},t)$, and concentration, $c(\vec{r},t)$. On the top and bottom edges Dirichlet boundary conditions for electric potential of 1.0 V and 0 V are imposed, respectively. Dirichlet boundary conditions for concentration are imposed on the top and bottom edges for an ideal electrical contact. The initial conducting and non-conducting regions are separated by an interface located at 4 nm from the bottom contact. The initial concentration,

[3]The functional spatial and time dependence of $V(\vec{r},t)$ and $c(\vec{r},t)$ has been dropped for Equation 4.6a

$c(\vec{r}, 0)$, is uniformly distributed between 0.1 and 0.3 for the non-conducting state and 0.7 and 0.9 for the conducting state, to approximate the pristine thin-film structure shown in Figure 4.2. The double-well potential, A, is set to 1.0 eV; the interfacial gradient energy term, κ, is set to 5.0 eV/nm^2; mobility, M, is set for 0.1 $nm^2/(V \times ns)$ [65],[66],[67],[68]. Convergence was defined by reaching a total energy minimum.

4.3 Discussion

An initial simulation was performed on an ideal abrupt interface to study the impact of interface roughness on the initial growth process of the conducting channel, as illustrated by the initial and final states illustrated by Figures 4.3a and 4.3b, respectively. The initial concentration of the conducting and non-conducting states of the structure were set uniformly to 0.7 and 0.3, respectively, thereby forming an abrupt interface with no roughness. As seen in Figure 4.3b, no conducting channel growth was observed, which suggests that the formation of conducting channels that bridge the top and bottom contacts is not energetically favored if the initial interface is abrupt. In other words, conducting channels may form if the initial interface has a certain level of roughness, which is consistent with experiments in which an interface separating two domains always have roughness. While the initial interface of Figure 4.3a appears to be morphologically abrupt, interface roughness in our modeling relates to the magnitude of the variation in $c(\vec{r}, 0)$ along the interface. An abrupt interface obtains when $c(\vec{r}, 0)$ is constant within the conducting and non-conducting states and a diffuse interface ob-

tains when $c(\vec{r}, 0)$ varies within each of the two regions, as they do with initial conditions illustrated by Figure 4.2.

Using the pristine initial conditions specified by Figure 4.2, illustrated by Figure 4.3c, the self-consistent solution of Equations 4.6a and 4.6b for concentration, $c(\vec{r}, t)$, is shown by Figure 4.3d. The results show formation of several conducting clusters and one continuous conducting channel, distinguished by the conducting domains shown in red and the non-conducting domains shown in blue. These results suggest unique interface microstructure develops from the initial interface under the influence of electrical potential and leading to the birth of distinctive conducting domains running through the non-conducting states. Note the presence of a continuous conducting channel traversing the bottom edge to the top edge of the thin film structure, as well as the presence of incomplete and orphaned conducting domains. The presence of a continuous conducting channel suggests the existence of an electroformed state, for the particular conditions of the present simulation.

The equilibrium interface formed by the conducting state and non-conducting state intrinsically describes the morphology of the conducting channel, represented by an envelope of cluster-like domains composed of many discrete charge carriers. The minimum energy condition imposed by the variation of the free-energy functional Equation 4.3 reflects local equilibrium between bulk free-energy density, interface energy, and their interaction with the applied electric potential, subject to appropriate boundary conditions and material properties.

To explore the influence of film thickness on the formation of conducting chan-

nels, an additional simulation was carried out on an otherwise identical thin film structure 50 nm thick, as shown by Figure 4.3e. Figure 4.3f shows the self-consistent solution for concentration, $c(\vec{r}, t)$, under these new conditions. It is evident that while formation of several conducting channel-like clusters has occurred, there does not appear to be a continuous conducting channel traversing the bottom edge to the top edge of the thin film structure. In further contrast, there appears to be relatively more incomplete and orphaned conducting domains.

The thickness-to-width ratio for the structures of Figures 4.3c and 4.3e is 0.2 and 1.0, respectively. This suggests an affinity for conducting channel formation for low thickness-to-width ratios, perhaps because of the dominance of the bulk free-energy, as indicated by the free-energy functional Equation 4.3. This observation has also been previously suggested based on experimental observations the formation of conducting channels depends substantially on the relative aspect ratio of the thin film structure as well as a numerous experiments that seem to indicate that a dielectric thin film needs to be in the range of 1 nm to 10 nm for conducting channels to form[14].

4.4 Summary

A computational phase field study of thin film conducting channel morphology and evolution has been presented. Atomic metastable states of thin films, responsible for resistance switching behavior, produces complex microstructure resulting from interaction of bulk free-energy and interface energy. The phase field formulation naturally

avoids the mathematically onerous problem of tracking the dynamical evolution of the interface formed by this microstructure.

Our computational results suggest the phase field formulation can model the dynamical evolution of conducting channel formation and growth, illustrating a new method for the study of dielectric thin films for resistive switching. Our results further suggest that only when the initial interface has roughness do conducting channels form. Since interface roughness is expected to exist in any real dielectric thin film interface, we thus expect to observe switching in many films.

Furthermore, even though an initial well-prepared interface will exhibit finite roughness, the film thickness needs to be thin enough for a conducting channel to form, consistent with experimental data from thin film structures having a thickness-to-width ratio substantially less than unity. Physically this makes sense insofar as the lateral dimension establishes the number of nucleation sites at which conducting channels start forming, *i.e.* if the lateral dimension is extremely small, there exists reduced likelihood of conducting channel formation.

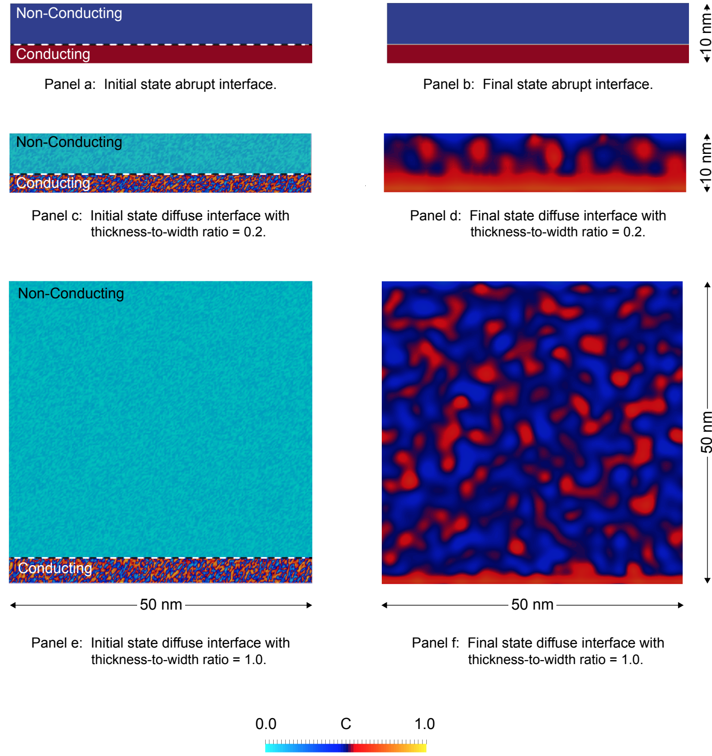

Figure 4.3: Initial state and the final state self-consistent solution of Equations 4.6a and 4.6b for concentration, $c(\vec{r}, t)$. The initial interface is formed 4 nm from the bottom contact. Panel (a) shows an ideal abrupt interface, defined as $c(\vec{r}, 0)$ being constant within the conducting and non-conducting regions, with panel (b) showing the resultant solution for $c(\vec{r}, t)$. The initial conditions of this abrupt interface are established by uniformly setting the conducting and non-conducting concentrations of the structure to 0.7 and 0.3, respectively. In this case, no conducting channel growth was observed, suggesting formation of conducting channels that bridge the top and bottom contacts is not energetically favored if the initial interface is abrupt. Panel (c) shows a diffuse interface, established by an initial concentration, $c(\vec{r}, 0)$, uniformly distributed between 0.1 and 0.3 for the non-conducting state and 0.7 and 0.9 for the conducting state, reproducing the pristine thin-film structure shown in Figure 4.2. Panel (d) showing the resultant solution for $c(\vec{r}, t)$, showing formation of several conducting clusters and one continuous conducting channel, distinguished by the conducting domains shown in red and the non-conducting domains shown in blue. Panel (e) applies the initial conditions of panel (c) to a 50 nm $\times$ 50 nm structure, with the resultant solution for $c(\vec{r}, t)$ shown by panel (f). It is evident that while formation of several conducting channel-like clusters has occurred, there does not appear to be a continuous conducting channel traversing the bottom edge to the top edge of the thin film structure.

Chapter 5

Conclusion and Future Directions

This dissertation has successfully produced a computational phase field study of the dynamical evolution of conducting channel formation of resistive switching dielectric thin films. With the phase field method, the assumptions of an *a priori* conducting channel model and the presence of specific transport phenomena to explain resistive switching are abandoned, and the model is instead formulated as a diffuse interface problem subject to a variational principle. The isothermal phase field formulation successfully predicts formation of conducting channels in typical dielectric thin film structures comparable to a range of resistive switches, offering an alternative computational approach based on metastable states treated at the atomic scale, requiring no assumptions on conducting channel morphology and its fundamental transport mechanisms.

The following publications were produced from the research of the present dissertation.

- J. F. Sevic and N. P. Kobayashi, A Computational Phase Field Study of Conduct-

ing Channel Formation in Dielectric Thin Films: A View Towards the Physical Origins of Resistive Switching, In review with Applied Materials and Interfaces.

- J. F. Sevic and N. P. Kobayashi, Self-consistent continuum- based transient simulation of electroformation of niobium oxide tantalum dioxide selector-memristor structures, Journal of Applied Physics 124, 164501 (2018).
- J. F. Sevic and N. P. Kobayashi, Multi-physics transient simulation of monolithic niobium dioxide-tantalum dioxide memristor selector structures, Applied Physics Letters 111, 153107 (2017).
- J. Sevic, and N. Kobayashi, "Multiphysics FEM study of TaO_2-NbO_2 thin-film electroforming," SPIE, **10349** San Diego (2017).
- J. Diaz-Leon, K. Norris, J. Yang, J. Sevic, and N. Kobayashi, A niobium oxide-tantalum oxide selector- memristor self-aligned nanostack, Applied Physics Letters, 110, 103102 (2017).
- J. Diaz-Leon, K. Norris, J. Sevic, and N. Kobayashi, Integration of a niobium oxide selector on a tantalum oxide memristor by local oxidation using joule heating, SPIE, **9924** San Diego (2016).

@proceeding author = Juan J. Daz Len,Kate J. Norris,John F. Sevic,Nobuhiko P. Kobayashi, title = Integration of a niobium oxide selector on a tantalum oxide memristor by local oxidation using Joule heating, volume = 9924, year = 2016, doi = 10.1117/12.2239609, URL = https://doi.org/10.1117/12.2239609, eprint =

Since the primary objective of the present dissertation is to investigate the suitability of a phase field formulation for the computational study of conducting channel formation of resistive switching dielectric thin films, certain assumptions were made to simplify the problem. Specifically, the isothermal assumption must be revisited, with the appropriate thermal transport mechanisms self-consistently coupled to the phase field and charge conservation equations. Moreover, an appropriate temperature dependence of bulk free-energy must be identified, *i.e.* a bivariate bulk free-energy function exhibiting dependence on both solute concentration and instantaneous temperature.

Bibliography

[1] D. Ielmini, "Resistive switching memories based on metal oxides: mechanisms, reliability and scaling," *Semiconductor Science and Technology*, vol. 31, p. 063002, may 2016.

[2] G. Gibson, S. Musunuru, J. Zhang, K. Vandenberghe, J. Lee, C. Hsieh, W. Jackson, Y. Jeon, D. Henze, Z. Li, and R. Williams, "An accurate locally active memristor model for s-type negative differential resistance in nbox," *Applied Physics Letters*, vol. 108, p. 023505, Jan. 2016.

[3] F. Nardi, S. Larentis, S. Balatti, D. Gilmer, and D. Ielmini, "Resistive switching by voltage-driven ion migration in bipolar rram - part i: Experimental study," *IEEE Trans. on Electron Devices Letters*, vol. 59, no. 9, pp. 2461–2467, 2012.

[4] S. Larentis, F. Nardi, S. Balatti, D. Gilmer, and D. Ielmini, "Resistive switching by voltage-driven ion migration in bipolar rram - part ii: Modeling," *IEEE Trans. on Electron Devices Letters*, vol. 59, no. 9, pp. 2468–2475, 2012.

[5] S. Kim, S. Kim, K. M. Kim, S. R. Lee, M. Chang, E. Cho, Y.-B. Kim, C. J. Kim, U. In Chung, and I.-K. Yoo, "Physical electro-thermal model of resistive switching

in bi-layered resistance-change memory," *Scientific Reports*, vol. 3, pp. 1680 – 1686, 04 2013.

[6] J. Diaz-Leon, K. Norris, J. Yang, J. Sevic, and N. Kobayashi, "Integration of a niobium oxide selector on a tantalum oxide memristor by local oxidation using joule heating," *SPIE, San Diego*, 2016.

[7] J. Diaz-Leon, K. Norris, J. Yang, J. Sevic, and N. Kobayashi, "A niobium oxide-tantalum oxide selector-memristor self-aligned nanostack," *Appl. Phys. Lett.*, vol. 110, p. 103102, 2017.

[8] J. F. Sevic and N. P. Kobayashi, "Multi-physics transient simulation of monolithic niobium dioxide-tantalum dioxide memristor selector structures," *Applied Physics Letters*, vol. 111, no. 15, p. 153107, 2017.

[9] J. F. Sevic and N. P. Kobayashi, "Self-consistent continuum-based transient simulation of electroformation of niobium oxide tantalum dioxide selector-memristor structures," *Journal of Applied Physics*, vol. 124, no. 16, p. 164501, 2018.

[10] N. Xu, L. Liu, X. Sun, X. Liu, D. Han, Y. Wang, R. Han, J. Kang, and B. Yu, "Characteristics and mechanism of conduction/set process in titanium nitride-zinc oxide-platinum resistance switching random-access memories," *Applied Physics Letters*, vol. 92, no. 23, p. 232112, 2008.

[11] F. Pan, C. Chen, Z. shun Wang, Y. chao Yang, J. Yang, and F. Zeng, "Nonvolatile

resistive switching memories-characteristics, mechanisms and challenges," *Progress in Natural Science: Materials International*, vol. 20, pp. 1 – 15, 2010.

[12] D. Ielmini, "Modeling the universal set/reset characteristics of bipolar rram by field- and temperature driven filament growth," *IEEE Trans. Electron Devices*, vol. 58, p. 4309, 2011.

[13] T. Ahmed, S. Walia, E. L. Mayes, R. Ramanathan, P. Guagliardo, V. Bansal, M. Bhaskaran, J. J. Yang, and S. Sriram, "Inducing tunable switching behavior in a single memristor," *Applied Materials Today*, vol. 11, pp. 280 – 290, 2018.

[14] D. B. Strukov, G. S. Snider, D. R. Stewart, and R. S. Williams, "The missing memristor found," *Nature*, vol. 453, pp. 80 EP –, 05 2008.

[15] K. M. Kim, T. H. Park, and C. S. Hwang, "Dual conical conducting filament model in resistance switching tio2 thin films," *Scientific Reports*, vol. 5, pp. 7844 EP –, 01 2015.

[16] W. J. Boettinger, J. A. Warren, C. Beckermann, and A. Karma, "Phase-field simulation of solidification," *Annual Review of Materials Research*, vol. 32, no. 1, pp. 163–194, 2002.

[17] L.-Q. Chen, "Phase-field models for microstructure evolution," *Annual Review of Materials Research*, vol. 32, no. 1, pp. 113–140, 2002.

[18] Q. C. Sherman and P. W. Voorhees, "Phase-field model of oxidation: Equilibrium," *Phys. Rev. E*, vol. 95, p. 032801, Mar 2017.

[19] W. Shen, N. Kumari, G. Gibson, Y. Jeon, D. Henze, S. Silverthorn, C. Bash, and S. Kumar, "Effect of annealing on structural changes and oxygen diffusion in amorphous hfo2 using classical molecular dynamics," *Journal of Applied Physics*, vol. 123, no. 8, p. 085113, 2018.

[20] N. Provatas and K. Elder, *Phase-Field Methods in Materials Science and Engineering*. Weinheim, Germany: Wiley-VCH Verlag, 2010.

[21] J. Borghetti, Z. Li, J. Straznicky, X. Li, D. Ohlberg, W. Wu, D. Stewart, and R. Williams, "A hybrid nanomemristor/transistor logic circuit capable of self-programming," *Proceedings of the National Academy of Sciences of the United States of America*, vol. 106, pp. 1699–1703, 2009.

[22] S. Jo, T. Chang, I. Ebong, P. Mazumder, and W. Lu, "Nanoscale memristor device as synapse in neuromorphic systems," *Nano Letters*, vol. 10, no. 4, pp. 1297–1301, 2010.

[23] Y. Chen, "Highly scalable hafnium oxide memory with improvements in resistive distribution and read disturb immunity," *Digest of the IEEE International Electron Devices Society (2009)*, pp. 460–463, 2009.

[24] J. Augustynski, F. Grosse, D. Kumar, F. Sanchez, C. Santato, X. Sun, A. Vomiero, T. Yamamoto, K. Norris, J. Yang, and N. Kobayashi, "Structural and chemical analysis of nanoscale resistive switching devices: Assessment on nonlinear properties," *Cambridge University Press*, vol. 1805, 008 2015.

[25] S. H. Chang, S. C. Chae, S. B. Lee, C. Liu, T. W. Noh, J. S. Lee, B. Kahng, J. H. Jang, M. Y. Kim, D.-W. Kim, and C. U. Jung, "Effects of heat dissipation on unipolar resistance switching in platinum-niobium oxide-platinum capacitors," *Applied Physics Letters*, vol. 92, no. 18, p. 183507, 2008.

[26] M. Noman, A. Sharma, Y. Lu, M. Skowronski, P. Salvador, and J. Bain, "Transient characterization of the electroforming process in tio_2 based resistive switching devices," *Applied Physics Letters*, vol. 102, 2013.

[27] D. Cassidy, J. Fox and A. Betts, "A model for the voltammetric behaviour of tio2 memristors," *Journal of Solid State Electrochemistry*, vol. 5, no. 20, pp. 1229–1234, 2016.

[28] S. K. Nandi, X. Liu, D. K. Venkatachalam, and R. G. Elliman, "Self-assembly of an nbo2 interlayer and configurable resistive switching in pt/nb/hfo2/pt structures," *Applied Physics Letters*, vol. 107, no. 13, p. 132901, 2015.

[29] C. H. Henager and W. T. Pawlewicz, "Thermal conductivities of thin, sputtered optical films," *Appl. Opt.*, vol. 32, pp. 91–101, Jan 1993.

[30] D. Flynn and M. O'Hagan, "Measurements of the thermal conductivity and electrical resistivity of platinum," *Journal of Research of the National Bureau of Standards*, vol. 71, Aug 1967.

[31] J. W. Arblaster, "The thermodynamic properties of platinum in its-90," *Platinum Metals Review*, vol. 38, 1994.

[32] IAEA, ed., *THERMOPHYSICAL PROPERTIES OF MATERIALS FOR NUCLEAR ENGINEERING: A TUTORIAL AND COLLECTION OF DATA IAEA*. Vienna: International Atomic Energy Association, 2008.

[33] K. Kelley, "The specific heats at low temperatures of tantalum oxide and tantalum carbide," *Journal of the American Chemical Society*, vol. 62, no. 4, pp. 818–819, 1940.

[34] S. M. Sze, *Physics of Semiconductor Devices*. New York: Wiley Interscience, 1981.

[35] A. S. Grove, *Physics and Technology of Semiconductor Devices*. New York: Wiley, 1967.

[36] D. Gaston, C. Newman, G. Hansen, and D. Lebrun-Grandié, "Moose: A parallel computational framework for coupled systems of nonlinear equations," *Nuclear Engineering and Design*, vol. 239, no. 10, pp. 1768–1778, 2009.

[37] S. Balay, S. Abhyankar, M. F. Adams, J. Brown, P. Brune, K. Buschelman, L. Dalcin, V. Eijkhout, W. D. Gropp, D. Kaushik, M. G. Knepley, L. C. McInnes, K. Rupp, B. F. Smith, S. Zampini, H. Zhang, and H. Zhang, "PETSc users manual," Tech. Rep. ANL-95/11 - Revision 3.7, Argonne National Laboratory, 2016.

[38] B. S. Kirk, J. W. Peterson, R. H. Stogner, and G. F. Carey, "`libMesh`: A C++ Library for Parallel Adaptive Mesh Refinement/Coarsening Simulations," *Engineering with Computers*, vol. 22, no. 3–4, pp. 237–254, 2006.

[39] J. Zhang, K. J. Norris, G. Gibson, D. Zhao, K. Samuels, M. M. Zhang, J. J.

Yang, J. Park, R. Sinclair, Y. Jeon, Z. Li, and R. S. Williams, "Thermally induced crystallization in niobium dioxide thin films," *Scientific Reports*, vol. 6, pp. 34294 EP –, 09 2016.

[40] B. Geist, "An experimental and theoretical investigation of minimization of forming-induced variability in resistive memory devices," *Department of Electrical Engineering Graduate Seminar, University of California, Santa Barbara*, 2012.

[41] S. Slesazeck, H. Mahne, H. Wylezich, A. Wachowiak, J. Radhakrishnan, A. Ascoli, R. Tetzlaff, and T. Mikolajick, "Physical model of threshold switching in nbo2 based memristors," *RSC Adv.*, vol. 5, pp. 102318–102322, 2015.

[42] F. Carsten, M. Stephan, A. Nabeel, Z. Hehe, H. Alexander, W. Rainer, and H. Susanne, "Multidimensional simulation of threshold switching in nbo2 based on an electric field triggered thermal runaway model," *Advanced Electronic Materials*, vol. 2, no. 7, p. 1600169.

[43] X. Liu, S. Li, S. K. Nandi, D. K. Venkatachalam, and R. G. Elliman, "Threshold switching and electrical self-oscillation in niobium oxide films," *Journal of Applied Physics*, vol. 120, no. 12, p. 124102, 2016.

[44] J. M. Goodwill, A. A. Sharma, D. Li, J. A. Bain, and M. Skowronski, "Electro-thermal model of threshold switching in taox-based devices," *ACS Applied Materials & Interfaces*, vol. 9, no. 13, pp. 11704–11710, 2017.

[45] Z. Wang, S. Kumar, Y. Nishi, and H.-S. P. Wong, "Transient dynamics of nbox

threshold switches explained by poole-frenkel based thermal feedback mechanism," *Applied Physics Letters*, vol. 112, no. 19, p. 193503, 2018.

[46] K. Jung, Y. Kim, W. Jung, H. Im, B. Park, J. Hong, J. Lee, J. Park, and J.-K. Lee, "Electrically induced conducting nanochannels in an amorphous resistive switching niobium oxide film," *Applied Physics Letters*, vol. 97, no. 23, p. 233509, 2010.

[47] K. Jung, Y. Kim, Y. S. Park, W. Jung, J. Choi, B. Park, H. Kim, W. Kim, J. Hong, and H. Im, "Unipolar resistive switching in insulating niobium oxide film and probing electroforming induced metallic components," *Journal of Applied Physics*, vol. 109, no. 5, p. 054511, 2011.

[48] J. M. Haile, *Molecular Dynamics Simulation: Elementary Methods.* New York, NY, USA: John Wiley & Sons, Inc., 1st ed., 1992.

[49] O. Madelung, *Introduction to Solid-State Theory.* Berlin, Germany: Springer Verlag, 1st ed., 1978.

[50] N. Mott and R. Gurney, *Electronic Processes and Ionic Crystals.* London, England: Oxford University Press, 1st ed., 1940.

[51] F. Chudnovskii, L. Odynets, A. Pergament, and G. Stefanovich, "Electroforming and switching in oxides of transition metals: The role of metal insulator transition in the switching mechanism," *Journal of Solid State Chemistry*, vol. 122, pp. 95–99, Feb. 1996.

[52] J. Crank, *Free and Moving Boundary Value Problems.* London, England: Oxford University Press, 1st ed., 1987.

[53] J. J. Yang, F. Miao, M. D. Pickett, D. A. A. Ohlberg, D. R. Stewart, C. N. Lau, and R. S. Williams, "The mchanism of electroforming of metal oxide memristive switches," *Nanotechnology*, vol. 20, no. 21, p. 215201, 2009.

[54] S. Kumar, Z. Wang, N. Davila, N. Kumari, K. J. Norris, X. Huang, J. P. Strachan, D. Vine, A. L. D. Kilcoyne, Y. Nishi, and R. S. Williams, "Physical origins of current and temperature controlled negative differential resistances in nbo2," *Nature Communications*, vol. 8, no. 1, p. 658, 2017.

[55] L. D. Landau and E. M. Lifshitz, *Statistical Physics.* Elmsford, New York: Pergamon Press, 3rd ed., 1980.

[56] N. F. Mott, "Metal-insulator transition," *Rev. Mod. Phys.*, vol. 40, pp. 677–683, Oct 1968.

[57] M. Imada, A. Fujimori, and Y. Tokura, "Metal-insulator transitions," *Rev. Mod. Phys.*, vol. 70, pp. 1039–1263, Oct 1998.

[58] R. Waser and M. Aono, "Nanoionics-based resistive switching memories," *Nature materials*, vol. 6, pp. 833–40, 12 2007.

[59] M. Seul and D. Andelman, "Domain shapes and patterns: The phenomenology of modulated phases," *Science*, vol. 267, no. 5197, pp. 476–483, 1995.

[60] Z. Hiroi, H. Hayamizu, T. Yoshida, Y. Muraoka, Y. Okamoto, J.-i. Yamaura, and Y. Ueda, "Spinodal decomposition in the tio2vo2 system," *Chemistry of Materials*, vol. 25, no. 11, pp. 2202–2210, 2013.

[61] J. P. Strachan, M. D. Pickett, J. J. Yang, S. Aloni, A. L. David Kilcoyne, G. Medeiros-Ribeiro, and R. Stanley Williams, "Direct identification of the conducting channels in a functioning memristive device," *Advanced Materials*, vol. 22, no. 32, pp. 3573–3577, 2010.

[62] F. Miao, J. P. Strachan, J. J. Yang, M.-X. Zhang, I. Goldfarb, A. C. Torrezan, P. Eschbach, R. D. Kelley, G. Medeiros-Ribeiro, and R. S. Williams, "Anatomy of a nanoscale conduction channel reveals the mechanism of a high-performance memristor," *Advanced Materials*, vol. 23, no. 47, pp. 5633–5640, 2011.

[63] J. W. Cahn and J. E. Hilliard, "Free energy of a nonuniform system. i. interfacial free energy," *The Journal of Chemical Physics*, vol. 28, no. 2, pp. 258–267, 1958.

[64] M. R. Tonks, D. Gaston, P. C. Millett, D. Andrs, and P. Talbot, "An object-oriented finite element framework for multiphysics phase field simulations," *Computational Materials Science*, vol. 1, no. 1, pp. 20 – 29, 2012.

[65] K. Stella, D. A. Kovacs, D. Diesing, W. Brezna, and J. Smoliner, "Charge transport through thin amorphous titanium and tantalum oxide layers," *Journal of The Electrochemical Society*, vol. 158, no. 5, pp. P65–P74, 2011.

[66] D. B. Strukov and R. S. Williams, "Exponential ionic drift: fast switching and low

volatility of thin-film memristors," *Applied Physics A*, vol. 94, pp. 515–519, Mar 2009.

[67] U. N. Gries, H. Schraknepper, K. Skaja, F. Gunkel, S. Hoffmann-Eifert, R. Waser, and R. A. De Souza, "A sims study of cation and anion diffusion in tantalum oxide," *Phys. Chem. Chem. Phys.*, vol. 20, pp. 989–996, 2018.

[68] T. Reed, *Free Energy of Formation of Binary Compounds.* Cambridge, MA: MIT Press, 1st ed., 1971.

Appendix A

Poole-Frenkel Conductivity Test Cases

This Appendix illustrates Poole-Frenkel bulk conductivity test cases based on Poole-Frenkel diffusion and mobility, as given by Equations A.1a and A.1b. The expected behavior is observed.

$$D_F(\vec{r}) = D_o exp(-\beta E_{ac}^{D}) \tag{A.1a}$$

$$\mu_F(\vec{r}) = \frac{1}{T} exp(-\beta E_{ac}^{\mu}) \tag{A.1b}$$

Here E_{ac}^{D} and E_{ac}^{μ} are activation energies for diffusion and drift, respectively.

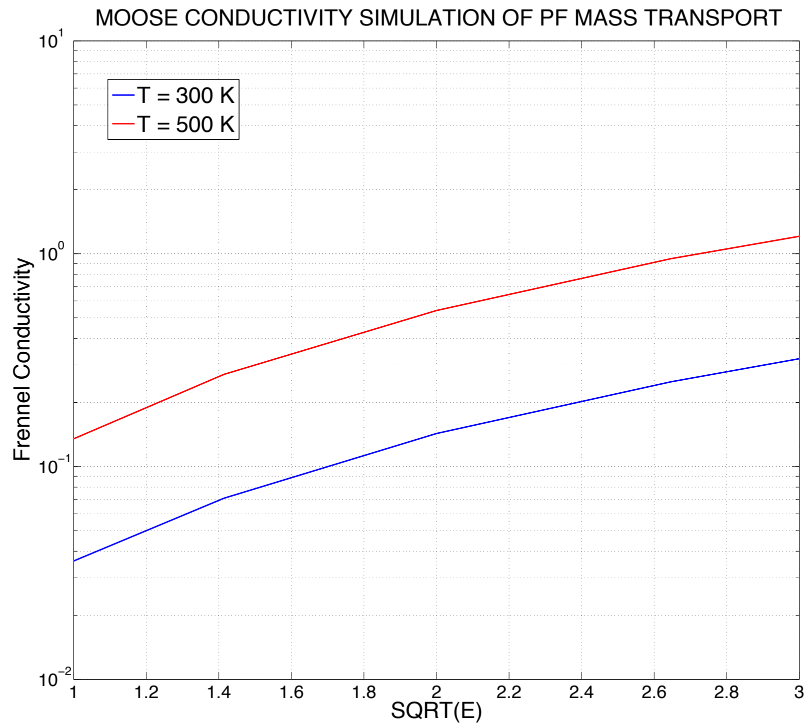

Figure A.1: Continuum test case of Poole-Frenkel conductivity versus square root of electric field.

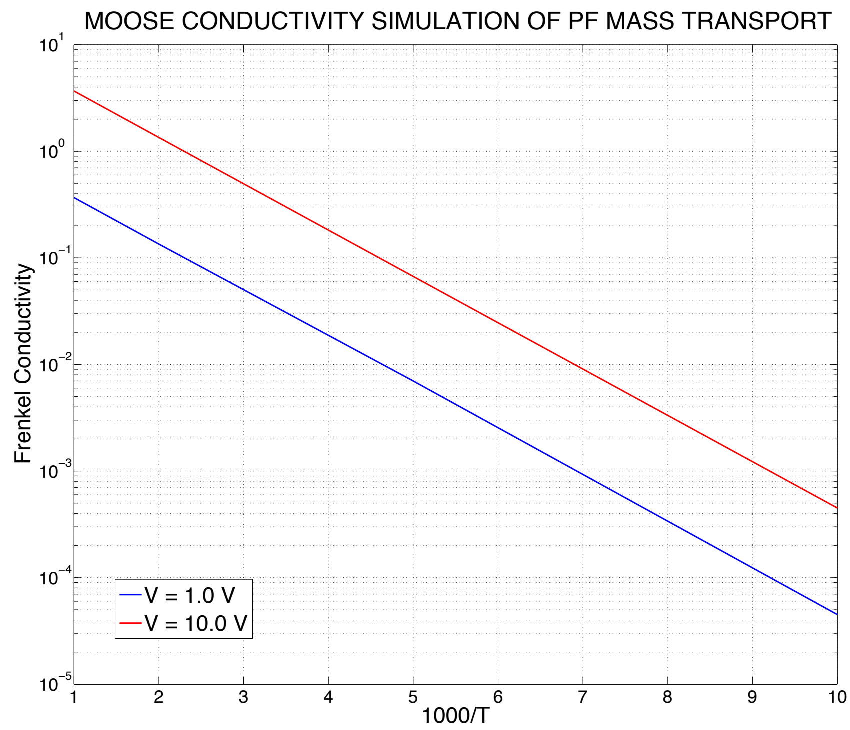

Figure A.2: Continuum test case of Poole-Frenkel conductivity versus inverse of temperature.

Appendix B

Phase Field Test Cases

This Appendix show the steady-state response for test-cases, to validate proper behavior of the electrostatic energy term, Equation B.1. Figure B.1 below shows two different bias conditions: top contact positive and bottom contact positive. The expected phenomena is observed.

$$g_{elec}(c,V) = \frac{q}{\Omega} V(\vec{r},t) c(\vec{r},t) \tag{B.1}$$

Panel a: Positive bias on top contact.

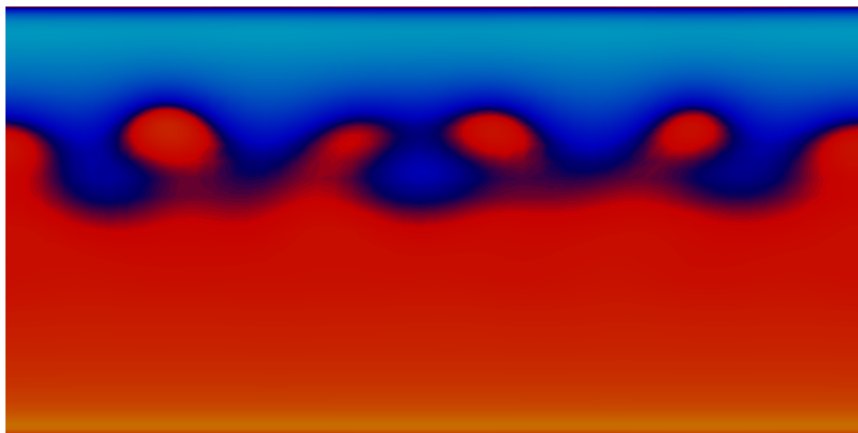

Panel b: Positive bias on bottom contact.

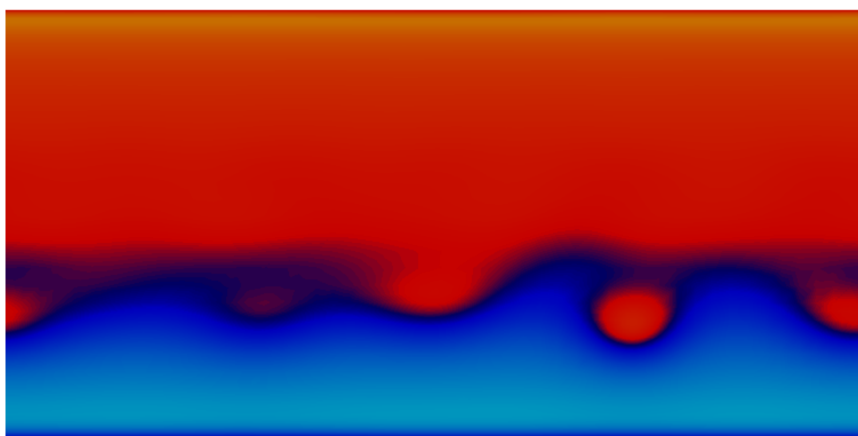

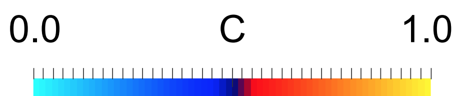

Figure B.1: Phase field test cases to validate electrostatic potential term.

Appendix C

Multiphysics Object Oriented Simulation Environment - MOOSE

Introduction

This Appendix introduces the Multiphysics Object-Oriented Simulation Environment (MOOSE) finite-element PDE solver framework [36]. Through an API, MOOSE provides an extensbible high-level framework to the PetSC nonlinear solver and libmesh mesher to solve a broad variety of partial differential equations typically encountered in engineering and physics. MOOSE was developed by the Idaho National Laboratory, while the PetSC [37] and libmemsh tools were developed at the Argrone and Sandia National Laboratories, respectively [38].

In contrast to commercial FEM tools, which are generally centered around a propreitary integrated design environment (IDE), the MOOSE workflow requires sev-

eral additional applications, including a C compiler and visualization tools. A central feature of the MOOSE framework is the weak form specification of physics kernels in C, providing a flexibe mechanism for the formulation of complex anisotropic and nonlinear contiuum and hydrodynamic flow problems.

A MOOSE workflow is presented, including installation instructions. A simual-tion example is provided to illustrate the application of MOOSE for self-consistent electrothermal simulation of a memristor structure.

What is MOOSE

MOOSE solves systems of coupled partical differential equations. Each PDE is cast into an associated weak formualtion of the fintie element method to represent and solve the coupled system on a discretized 2-D or 3-D mesh. For example, consider the heat equation with forcing term Q_f

$$\rho C_p \frac{\partial T}{\partial t} + \nabla \cdot \vec{k_T} \nabla T = Q_f \tag{C.1}$$

where ρ is mass density, C_p is (nonlinear) heat capacity, and $\vec{k_T}$ is (nonlinear and anisotropic) thermal conductance. The weak formulation is a variational statement on an element expressed, expressed in inner-product form as

$$\left(\psi, \rho C_p \dot{T}\right) + \left(\nabla\psi, \vec{k_T} \nabla T\right) = (\psi, Q_f) \tag{C.2}$$

where ψ is a test function that approximates the PDE solution over the ele-

ment. It is the weak form Eq. C.2 that is coded as a C object to represent physics of the problem that is solved by MOOSE. Each term of each PDE yields a kernel in C that is supplied to MOOSE and subsequently solved using iterative techniques.

Both steady-state and transient solvers are available. A major feature of MOOSE is the Newton-free Krylov solver, precluding the need for analytical Jacobian derivation or analytical computation. MOOSE outputs an industry-standard Exodus data file, suitable for visualization. Each of these steps are in general distinct and done with individual applications that make up the MOOSE workflow.

The MOOSE Workflow

This section discusses the minimum suite of applications to create an effective workflow, with a major feature being the broad discretion afforded in configuration. The MOOSE workflow depends largely on user preference, with a minimum workflow suite itemized below; each of these are disucssed in turn.

Following description of custom physics, using the weak form cast in C code, which requires compiling, the majority of the workflow centers around simulation specification by the MOOSE deck (text editor), executing the simulation (command line), and visualization (application).

- MOOSE application
- Text editor
- Mesh application

- Visualization application

- Compiler

The MOOSE Application

The MOOSE application is similar to Python or MATLAB in many ways, such as a command-line interface to an API (Application Program Interface). MOOSE must be complied when it is installed, unlike MATLAB, so a compiler is required. The resulting executable provides an API that executes a simulation described by a text-file in which custom physics are linked to MOOSE run-time by user-supplied C code. The MOOSE API is itself based on the PetSC PDE solver from Argonne National Lab and the libmesh framework from Sandia National Lab.

Text Editor

The text editor is the focal point of the MOOSE workflow, with the Atom being the endorsed text editor; a custom configuration file is avaiable for Atom for syntax highlighting for the MOOSE API. It is suggested to read `http://mooseframework.org/wiki/MooseTraining/InputFile/` for an introduction to basic elements of a MOOSE deck.

The Mesh Application

MOOSE requires that a mesh be supplied, inlcuding boundary and volume names. The libmesh framework from Sandia has a commercial version with academic

pricing, which was evaluated. Simultaneously, the Gmsh open-source mesher was evaluated and found to be suitable for introductory research; it is this mesher that is the focus of the present note. The Gmsh application has stable builds for Mac, Linux, and Windows.

The Visualization Application

The MOOSE install provides a basic GUI interface the API and includes basic visualiztion. MOOSE exports an industry standard Exodus file that can be read by many third-party visualization applications; for the present note, open-source ParaView delivered execeptional visualization capability.

Compliler

To invoke the MOOSE API, a machine-specific executable must be provided by a compiler. Moreover, custom physics in MOOSE must be compiled and linked to the MOOSE executable. Generally, once the physics are coded, no further compiling is necessary.

OSX Installation

This sections describes the El Captain OSX installation procedure for MOOSE, and the associated applications from the previous section, specifically the Atom text editor, the Gmsh mesher, the ParaView visualizer, and the gcc C compiler.

Optimum installation results with a clean OSX install, followed by the MOOSE install. The remaining applications can be installed in any order.

MOOSE Install

The El Captain OSX installation instructions are found at `http://mooseframework.org/getting-started/osx/`. Note that Xcode, with command line tools, must be installed prior to the MOOSE installation.

Following the MOOSE installation, go to `http://www.mooseframework.org/getting-started/` and follow the instructions for cloning MOOSE and and compiling libmesh. Compiling takes about an hour. Run the test suite to confirm MOOSE has been properly installed.

Atom Install

The Atom download is found at `https://atom.io`. It is recommended to install the MOOSE-specific syntax-highlighting package, found at `https://atom.io/packages/language-moose`.

Gmsh Install

The Gmsh download is found at `http://gmsh.info`. Note that Gmsh offers both 2-D and 3-D mesh support.

ParaView Install

The ParaView download is found at `http://www.paraview.org`.

Compiler Install

The X-Code installation will install gcc, an OSX-compatible C/C++ compiler. To verify correct installtion, type `cc --version` at an X-Term command line.

Simulation Example with MOOSE

This section provides the details necessary to self-consistently simulate transient and steady-state Joule self-heating of the memristor structure similar to that illustrated by Figure 2.2.

The Weak Formulation

To model Joule heating, the following PDEs are solved self-consistently

$$\rho C_p \frac{\partial T}{\partial t} + \nabla \cdot \vec{k_T} \nabla T - Q_f = 0 \tag{C.3a}$$

$$\nabla \cdot \sigma \nabla V = 0 \tag{C.3b}$$

where ρ is mass density, C_p is (nonlinear) heat capacity, $\vec{k_T}$ is (nonlinear and anisotropic) thermal conductance, and σ is (nonlinear) electrical conductance. Thermal and electric potential variables T and V, respecitvely, are 2-D functions of space and

time-dependent. Equations C.3a and C.3b are solved subject to the Joule heating coupling term that relates instantaneous power density to the thernal forcing term

$$Q_f = \sigma \left| \nabla V \right|^2 \tag{C.4}$$

The diffusion operator is the only built-in function provided by the MOOSE API [1]. To solve self-consisently Equations C.3a, C.3b, and C.4, requires a custom kernal for coupling, represetned by Q_f, and the intertial term, represented by $\rho C_p \dot{T}$. The following weak formulations obtain, respectively,

$$(\psi, \sigma\, u_h\, u_h) \tag{C.5a}$$

$$\left(\psi, \rho C_p \dot{T}\right) \tag{C.5b}$$

Kernel Implementation

Each kernel requires a header (.h) file with declarations and a code file (.c) that implements the weak formulation from the previous section. Each kernel must also be registered with the MOOSE (.c). A complete listing of MOOSE classes is available at `http://mooseframework.org/docs/doxygen/moose/classes.html`. Specfically the weak form Equation C.5a uses the coupledValue class, described here `http://mooseframework.org/docs/doxygen/moose/classCoupleable.html#adb2f4c4446e2100f486abeb2513c4f01`.

The C code fragment represting the weak formulation Equation C.5a is given immediately below, where u_h of Equation C.5a is represented in the function by `some_variable`.

[1] See `http://mooseframework.com/docs/syntax/moose/`

Note that the weak form is expressed as the LHS, so the (-1) term is necessary [2]. The material conductivity is passed by the variable `_diffusivity` which represents σ.

[2] In this code fragment, and the following two, not all the code has been included from the .c file, what is shown are the most important fragments.

```
#include "ExampleConvection.h"

template<>
InputParameters validParams<ExampleConvection>()
{
  InputParameters params = validParams<Kernel>();

  params.addRequiredCoupledVar("some_variable", "Some variable.");
  return params;
}

ExampleConvection::ExampleConvection(const InputParameters & parameters) :
    Kernel(parameters),
    _some_variable(coupledValue("some_variable")),
    _diffusivity(getMaterialProperty<Real>("diffusivity"))
{}

Real ExampleConvection::computeQpResidual()
{
  return _test[_i][_qp]*(_some_variable[_qp]*_some_variable[_qp])*(
      _diffusivity[_qp])*(-1);

}

Real ExampleConvection::computeQpJacobian()
{
```

```
  return _test[_i][_qp]*(_diffusivity[_qp]*_some_variable[_qp]*
      _some_variable[_qp]*_phi[_j][_qp])*(1);
}
```

The C code fragment representing the weak formulation Equation C.5b is given immediately below. Specific heat and density are passed by the variables `_specific_heat` and `_density`. Note that the time derivative function is called in the code. Further, and significantly, note that an analytical Jacobian is not required to be specified, a major feature of MOOSE.

```
#include "HeatConductionTimeDerivative.h"

template<>
InputParameters validParams<HeatConductionTimeDerivative>()

HeatConductionTimeDerivative::HeatConductionTimeDerivative(const
    InputParameters & parameters)
  : TimeDerivative(parameters),
   _use_heat_capacity(getParam<bool>("use_heat_capacity")),
   _specific_heat(NULL),
   _density(NULL)
{
}

Real
HeatConductionTimeDerivative::computeQpResidual()
{
  return (*_specific_heat)[_qp] * (*_density)[_qp] * TimeDerivative::
      computeQpResidual();
}

Real
HeatConductionTimeDerivative::computeQpJacobian()
{
  return (*_specific_heat)[_qp] * (*_density)[_qp] * TimeDerivative::
      computeQpJacobian();
```

```
}
```

The C code fragment kernel registration is shown immediately below, under the comment section for self-consistent electrothermal includes, illustrating various custom kernels and material definitions. Kernel implementation is concluded by compling the various code framgments and linking them the MOOSE executable; this is generally done with the `make` that comes with the MOOSE install. Each of the files must also be placed in their respective directories.

Passing Material Parameters

Material parameters are be passed to to the kernels of the previous section by using the material functions `HeatConductionMaterial` for passing thermal conductivity, specific heat, and density and `ExampleMaterial` for passing electrical conductivity. Material parameters are expressed as vectors / tensors from the MOOSE deck

The MOOSE Simulation Deck

The MOOSE simulation is specified by a text file composed of the following elements, which are discussed in turn. A complete summarty of MOOSE simulation elements and systems is located at `http://mooseframework.org/wiki/MooseSystems/` with parameter definitions located at `http://mooseframework.com/docs/syntax/moose/`.The MOOSE simulation deck is listed in Appendix A.

- Mesh

- Variables
- Mesh application
- Kernels
- Boundary Conditions
- Materials
- Executioner
- Output

```
#include "ExampleApp.h"
#include "Moose.h"
#include "Factory.h"
#include "AppFactory.h"

// Self-consistent electrothermal includes, March 21 2016
#include "ExampleConvection.h"
#include "ExampleMaterial.h"
#include "HeatConductionMaterial.h"
#include "HeatConduction.h"
#include "HeatConductionTimeDerivative.h"

template<>
InputParameters validParams<ExampleApp>()
{
  InputParameters params = validParams<MooseApp>();

  params.set<bool>("use_legacy_uo_initialization") = false;
  params.set<bool>("use_legacy_uo_aux_computation") = false;
  return params;
}

ExampleApp::ExampleApp(InputParameters parameters) :
    MooseApp(parameters)
{
  srand(processor_id());
```

```
  Moose::registerObjects(_factory);
  ExampleApp::registerObjects(_factory);

  Moose::associateSyntax(_syntax, _action_factory);
  ExampleApp::associateSyntax(_syntax, _action_factory);
}

ExampleApp::~ExampleApp()
{
}

void
ExampleApp::registerObjects(Factory & factory)
{
  // Register ExampleConvection even though it is a forcing term.
  registerKernel(ExampleConvection);

  // Register our new material class so we can use it.
  registerMaterial(ExampleMaterial);

  // Register the heat conduction kernel.
  registerKernel(HeatConductionKernel);

  // Register thermal material properties.
  registerMaterial(HeatConductionMaterial);
```

```
  // Register transient thermal kernel.
  registerKernel(HeatConductionTimeDerivative);
}
```

[Mesh]

The mesh is specified here, as a .msh file. MOOSE has basic commands to construct simple objects, rename boundaries and volumes, and resample the mesh.

[Variables]

Variables are defeind here, as well as the family of approximation functions the test function ψ belings to, the approximation order, and initial conditions.

[Kernels]

Kernels are defined here, by `type` and `variable`. In the present example, `HeatConductionKernel` and `HeatConductionTransient` represents the diffusion inerial terms, respectively, of Equation C.1. The forcing term of Equation C.1 is represented by `couplingKernel`. The electric potential is also represented by `HeatConductionKernel`.

[Boundary Conditions]

Boundary conditions are defined here, with both Dirchlet (constant temperature) and Neumann (constant flux) supported; custom boundary can also be defined,

e.g. periodic or absorbring. Boundary conditions are attached to mesh boundaries using `boundary`.

[Materials]

Material properties are specified here, with `block` used to attach a material property to a specific volume or doamin. Thermal properties are passed as a vector of terms specifying $\vec{k_T}$, C_p, and ρ. Electrical conductivity is passed a vector of idepdendent terms (T) and dependet terms.

[Executioner]

The simulation type is specified in the executioner block, with steady-state and transient specified by `steady` and `transient`, respectively. Additional options are also specified, similar to SPICE, e.g. time step and simulation duration.

[Output]

Output parameters are specified here.

Simulation Result

The following embedded movie illustrates the the transient results of the simulation. Immediately below the movie is the steady-state result.

Appendix D

MOOSE Isothermal Phase Field Source Code

This Appendix lists the source code for the three custom kernels for the phase field formulation of dielectric thin-film resistive switching phenomena. Although the heat transport kernel was complied and included, for the work presented in this dissertation, thermal resistance was set to zero, thereby inhibiting Joule heating. The Laplace kernel is coupled to phase field concentration, $c(\vec{r}, t)$, to couple this variable as a proxy for conductivity.

The source code for the following three kernels follows.

- Coupled Laplace kernel
- Thermal diffusion kernel
- Joule heating term for thermal diffusion kernel

```
// John F. Sevic
// Department of Electrical Engineering, UC Santa Cruz
// March 23, 2018

// This kernel returns the diffusion operator of electric potential V, it is
// derived from the CoupledLaplace.c code used in the continuum transport
    code.
// The present version couples concentration variable c, as a proxy for
// conductivity, for the moment. Eventually, this will be treated rigorously
// as conductivity, a smooth function between sigma_max and sigma_min, which
// in fact is arbitrary for the work at hand.

#include "CoupledLaplace.h"

template<>
InputParameters validParams<CoupledLaplace>()
{
  InputParameters params = validParams<Kernel>();
  params.addRequiredCoupledVar("coupled_c", "This is c.");
  return params;
}

CoupledLaplace::CoupledLaplace(const InputParameters & parameters) :
  Kernel(parameters),
  _coupled_c(coupledValue("coupled_c"))
{}
```

```
Real CoupledLaplace::computeQpResidual()
{
// For P-F investigation, make _D the effective conductivity based on c.
  _D = 1.0*_coupled_c[_qp];
  return
   _D*_grad_u[_qp]* _grad_test[_i][_qp];
}


Real CoupledLaplace::computeQpJacobian()
{
  return _D*_grad_phi[_j][_qp] * _grad_test[_i][_qp];
}
```

```
// John F. Sevic
// Department of Electrical Engineering, UC Santa Cruz
// April 16, 2017

// This kernel returns the diffusion operator on T of a metal whose
    electrical
// condutcivity is described by a relaxatiom time transport approximation
    that
// in turn is used to establish the metal's thermal conductivity, kappa, by
// invoking the W-F law. The kernel also provides for setting kappa using
// a material property.

#include "HeatTransportMetal.h"

template<>
InputParameters validParams<HeatTransportMetal>()
{
  InputParameters params = validParams<Diffusion>();
  params.addRequiredCoupledVar("coupled_T", "This is T.");
  return params;
}

HeatTransportMetal::HeatTransportMetal(const InputParameters & parameters) :
    Diffusion(parameters),
      _coupled_T(coupledValue("coupled_T"))
{}
```

```
Real HeatTransportMetal::computeQpResidual()

{

  _sigma = 1.0;

  _lorenz = 1.0;

  _kappa = 1e-5;

//  return _kappa*Diffusion::computeQpResidual();

  return _kappa*_grad_u[_qp]*_grad_test[_i][_qp];


}


Real HeatTransportMetal::computeQpJacobian()

{

//  return _kappa*Diffusion::computeQpJacobian();

return _kappa*_grad_phi[_j][_qp]*_grad_test[_i][_qp];

}
```

```
// John F. Sevic
// Department of Electrical Engineering, UC Santa Cruz
// April 16, 2017

// This kernel computes the electrothermal source term of the Fourier heat
// transport equation, representing self-consistently coupeld Joule
// heating. Electrical conductivity is computed from a relaxation time model
// that takes tau to compute mobility.

#include "ThermalCouplingConductor.h"

template<>
InputParameters validParams<ThermalCouplingConductor>()
{
  InputParameters params = validParams<Kernel>();
  params.addRequiredCoupledVar("coupled_V", "grad of this is E.");
  return params;
}

// Calculate the source term within the metalic contact, thus for
   conductivity
// we use relaxation time approximation for mobility. The negative sign
// indicates this is a source term on the LHS of the transport equation.

ThermalCouplingConductor::ThermalCouplingConductor(const InputParameters &
   parameters) :
```

```
    Kernel(parameters),
    _coupled_E(coupledGradient("coupled_V"))
{}

Real ThermalCouplingConductor::computeQpResidual()
{
  _sigma = 0;
  return (-1)*_sigma*_test[_i][_qp]*(_coupled_E[_qp]*_coupled_E[_qp]);
}

Real ThermalCouplingConductor::computeQpJacobian()
{
  return _sigma*_test[_i][_qp]*(_coupled_E[_qp]*_coupled_E[_qp]*_phi[_j][_qp
      ]);
}
```

Appendix E

MOOSE Phase Field Isothermal Deck

This Appendix shows the MOOSE deck for the self-consistent isothermal phase field formulation and solution of Equations E.1a and E.1b below.

$$\frac{\partial c(\vec{r},t)}{\partial t} = \boldsymbol{\nabla} \cdot M \nabla \left[\frac{\partial f_{bulk}(c)}{\partial c} - \boldsymbol{\nabla} \cdot \kappa \nabla c - \frac{q}{\Omega} V \right] \tag{E.1a}$$

$$\nabla \cdot \sigma \left[c(\vec{r},t) \right] \nabla V(\vec{r},t) = 0 \tag{E.1b}$$

The present simulation framework was constructed primarily to explore and validate the phase field formulation to study dielectric thin-film resistive switching phenomena. Many approximations were used, and in many cases, less emphasis was placed on absolute scaling of the state variables versus their relative ratios. While this leads to some unusual independent variable absolute values, the expected behavior was nevertheless observed.

```
# John F. Sevic
# Department of Electrical Engineering
# UC Santa Cruz
#
# March 20, 2018
# This is my first attempt at phase—field, and also my last paper. For the
# problem at hand, we have assumed an alloy composed of alpha and beta whose
# free—energy density is a double—well potential that interacts with an
# external electrtic potential, V.
#
# The idea is to select the correct free—energy density and mobility
    parameters
# to model an interface similar to that seen in thin—film of interest to
# Nobby, e.g. off—stochiometric TaO2. The example version of the present
    MOOSE
# example features a double—well free—energy density function and an
    arbitrary
# surface mobility function. Our objective is to add interaction with the
# applied external potential, V. All BC's are periodic, unless otherwise
    noted.
# Electric potential boundary counditions are Neumann on sides and Dirichlet
     on
# top—bottom. IC is specified as a random concentration, c.
#
# March 20, 2018
```

```
# Example simulation of an iron-chromium alloy at 500 C. Equilibrium
# concentrations are at 23.6 and 82.3 mol% Cr. Kappa value, free energy
    equation,
# and mobility equation were provided by Lars Hoglund. Solved using the
    split
# form of the Cahn-Hilliard equation.
#
# March 21, 2018
# Need to add kernel for interaction with electric potential V. For now,
    assume
# unit conductivity. After establishing the correct boundary conditions, the
# simulation converges. Good.
#
# March 23, 2018
# Added Laplace kernel and it works, after making sure scaling was correct.
# The simulation converged and showed the correct electric field solution
    for
# 1 V at the top plate and 0 V at the bottom plate. The interface solution
# showed the correct behavior.
#
# March 24, 2018
# Added electric potential coupling by augmenting the free-energy density
    RHS
# with a kernel that couples V to using the SplitCHParsed. The free-energy
# density contribution is calculated in eV/mol by scaling the contribution
# due to V by the atomic volume, Omega. This needs to be confirmed again by
```

```
# IDL.
#
# March 25, 2018
#
# Modified the Laplace kernel by adding coupling to concentration variable c
    ,
# which will be eventually used to extract conductivity for the Laplace
# equation.
#
# May 29. 2018
#
# A long break to work on the second paper's revisions. Main additions to
# the present work is adding an arbitrary double-well free-energy function
# and heat transport coupled to order parameter / concentration variable, c.
#
# June 2, 2018
# It appears I can add T to DerivativeParsedMaterial to specify an
# arbitrary g(c,T) surface for our memristive thin-film. All that remains
# is specifying a reasonable surface mobility and surface interface energy
# and addition of heat transport, adding T.
#
# June 4, 2018
# Added basic heat transport and ET coupling kernels. They compile and
    couple
# to the free-energy density function. It looks like it works in a general
# sense, adding heat transport set for minimal infuence. The results for the
```

```
# will be restricted to the isothermal case anyway, at T ~ 400 K. But, the
# heat transport kernel works and is coupled to Joule heating. It is
   possible
# a source term may be necessary on its RHS for latent heat, especially as a
# function of the phase-field variable.
#
# August 17, 2018
# Final results. We are getting the results we expect, need to ensure all
# of the model calibrations are physical and have the correct units.
#
# August 21, 2018
# Have the ball-park parameters for A, kappa, and mu, and also justify the
# 10 nm x 100 nm grid, since a CF may be ~ 10 nm diameter.
#
# September 7, 2018
# This the MOOSE deck for final PhD publication. Even though the self-
   heating
# kernel is present, the coupling is set for ~0, so the simulation is
# isothermal, at T = 400 K. To test the theory that random spatial
   variations
# lead to a non-smooth interface, but at minimum enthalpy, we use various
# seed values for the concentration IC. The idea is this type of IC has the
# most initial randomness but we stil converve to non-smooth interface
# solutions at minimum enthalpy.
#
# September 28, 2018
```

```
# Made two final adjustments to simulation to enhance creation of
    filamentary
# interface: the interface diffusion constant was increased by 10x to reduce
# simulation time, and the free—energy density was reduced by 10x to better
# interact with the interface—energy density and electric field energy
    density.

# Janaury 6, 2019
# Ran one final sim with a mathematiclaly flat interface to illustrate
# mathematiclaly that no nucleation or channel growth occurs. Had already
# done this earlier, but did not save results. Changes are made only to IC.


[Mesh]
  type = GeneratedMesh
  dim = 2
  distribution = DEFAULT
  elem_type = QUAD4
  nx = 50
  ny = 50#10
  nz = 0
  xmin = 0
  xmax = 50
  ymin = 0
  ymax = 50#10
  zmin = 0
```

```
  zmax = 0
  uniform_refine = 2
[]

[GlobalParams]
  block = 0
[]


[Variables]
  [./c]   # Mole fraction of Cr (unitless)
    order = FIRST
    family = LAGRANGE
  [../]
  [./w]   # Chemical potential (eV/mol)
    order = FIRST
    family = LAGRANGE
  [../]
  [./V]   # Electric potential (V)
    order = FIRST
    family = LAGRANGE
  [../]
  [./T]   # Temperature (T)
    order = FIRST
    family = LAGRANGE
  [../]
```

```
[]

[AuxVariables]
  [./f_density]   # Local energy density (eV/mol)
    order = CONSTANT
    family = MONOMIAL
  [../]
[]

[ICs]
  [./concentrationIC]
    #type = RandomIC
    type = RndBoundingBoxIC
    x1 = 0
    y1 = 0
    x2 = 50
    y2 = 4
    mx_invalue = 0.65#0.8#0.9
    mn_invalue = 0.3#0.8#0.1
    mx_outvalue = 0.1#0.2
    mn_outvalue = 0.0#0.2#0.1
    variable = c
  [../]
  [./tempIC]
```

```
    type = RandomIC
    min = 399
    max = 401
    seed = 101
    variable = T
  [../]
[]

[BCs]
  [./Periodic]
    [./c_bcs]
      variable = c
      auto_direction = 'x y'
    [../]
    [./w_bcs]
      variable = w
      auto_direction = 'x y'
    [../]
    [./V_bcs]
      variable = V
      auto_direction = 'x'
    [../]
    [./T_bcs]
      variable = T
      auto_direction = 'x'
    [../]
```

```
  [../]
  [./V_top]
    type = DirichletBC
    variable = V
    boundary = 'top'
    value = 10e-6
  [../]
  [./V_bottom]
    type = DirichletBC
    variable = V
    boundary = 'bottom'
    value = 0.0
  [../]
  [./T_top]
    type = DirichletBC
    variable = T
    boundary = 'top'
    value = 400
  [../]
  [./T_bottom]
    type = DirichletBC
    variable = T
    boundary = 'bottom'
    value = 400
  [../]
[]
```

```
[Kernels]
  [./w_dot]
    variable = w
    v = c
    type = CoupledTimeDerivative
  [../]
  [./coupled_res]
    variable = w
    type = SplitCHWRes
    mob_name = M
  [../]
  [./coupled_parsed]
    variable = c
    type = SplitCHParsed
    f_name = f_loc
    kappa_name = kappa_c
    w = w
  [../]
  [./coupled_parsed_elec]
    variable = c
    type = SplitCHParsed
    f_name = f_ele
    kappa_name = kappa_e
    w = w
    args = 'c V'
```

```
  [../]
  [./laplace]
    variable = V
    type = CoupledLaplace
    coupled_c = c
  [../]
  [./HeatConduction]
    type = HeatTransportMetal
    variable = T
    coupled_T = T
  [../]
  [./ThermalCoupling]
    type = ThermalCouplingConductor
    variable = T
    coupled_V = V
  [../]
  [./T_dot]
    variable = T
    type = TimeDerivative
  [../]
[]


[AuxKernels]
  # Calculates the energy density by combining the local and gradient
      energies
```

```
  [./f_density]   # (eV/mol/nm^2)
    type = TotalFreeEnergy
    variable = f_density
    f_name = 'f_loc'
    kappa_names = 'kappa_c'
    interfacial_vars = c
  [../]
[]


[Materials]
  # d is a scaling factor that makes it easier for the solution to converge
  # without changing the results. It is defined in each of the first three
  # materials and must have the same value in each one.
  [./kappa]                  # Gradient energy coefficient (eV nm^2/mol)
    type = GenericFunctionMaterial
    # kappa_c *eV_J*nm_m^2* d
    prop_names = 'kappa_c'
    prop_values = '8.125e-16*6.24150934e+18*1e+09^2*1e-27'
  [../]
  [./kappa_e]
    # kappa_e *eV_J*nm_m^2* d
    type = GenericFunctionMaterial
    prop_names = 'kappa_e'
    prop_values = '5e-10'
  [../]
```

```
[./mobility]
  # Mobility (nm^2 mol/eV/s)
  type = DerivativeParsedMaterial
  f_name = M
  args = 'c'
  constant_names =       'Acr    Bcr    Ccr    Dcr
                          Ecr    Fcr    Gcr
                          Afe    Bfe    Cfe    Dfe
                          Efe    Ffe    Gfe
                          nm_m   eV_J   d'
  constant_expressions = '-32.770969 -25.8186669 -3.29612744 17.669757
                          37.6197853 20.6941796  10.8095813
                          -31.687117 -26.0291774 0.2286581   24.3633544
                          44.3334237 8.72990497  20.956768
                          1e+09      6.24150934e+18          1e-27'
  function = 'nm_m^2/eV_J/d*((1-c)^2*c*10^
              (Acr*c+Bcr*(1-c)+Ccr*c*log(c)+Dcr*(1-c)*log(1-c)+
              Ecr*c*(1-c)+Fcr*c*(1-c)*(2*c-1)+Gcr*c*(1-c)*(2*c-1)^2)
              +c^2*(1-c)*10^
              (Afe*c+Bfe*(1-c)+Cfe*c*log(c)+Dfe*(1-c)*log(1-c)+
              Efe*c*(1-c)+Ffe*c*(1-c)*(2*c-1)+Gfe*c*(1-c)*(2*c-1)^2))'
  # Scale mobility function by 10x to speed up simulation time.
  derivative_order = 1
  enable_jit = true
[../]
[./local_energy]
```

```
    # Local free energy function (eV/mol).
    type = DerivativeParsedMaterial
    f_name = f_loc
    args = 'c T'
    constant_names = 'A   B   C   D   E   F   G  eV_J  d'
    constant_expressions = '-2.446831e+04 -2.827533e+04 4.167994e+03
        7.052907e+03
                            1.208993e+04 2.568625e+03 -2.354293e+03
                            6.24150934e+18 1e-27'
    function = '10*eV_J*d*(A*c+B*(1-c)+C*c*log(c)+D*(1-c)*log(1-c)+
                E*c*(1-c)+F*c*(1-c)*(2*c-1)+G*c*(1-c)*(2*c-1)^2)'
#    function = '10*eV_J*d*((c-0.0)^2)*((c-1.0)^2)'
    derivative_order = 2
    enable_jit = true
  [../]
  [./electric_field_energy_density]
    # Electric potential contribution to local free-energy density (eV/mol).
    type = DerivativeParsedMaterial
    f_name = f_ele
    args = 'c V'
    constant_names = 'J_eV A B'
    constant_expressions = '1.6e-19 1.0e+19 1e4'
    function = 'V*c'
    derivative_order = 2
    enable_jit = true
  [../]
```

```
[]

[Postprocessors]
  [./step_size]             # Size of the time step
    type = TimestepSize
  [../]
  [./iterations]            # Number of iterations needed to converge
      timestep
    type = NumNonlinearIterations
  [../]
  [./nodes]                 # Number of nodes in mesh
    type = NumNodes
  [../]
  [./evaluations]           # Cumulative residual calculations for
      simulation
    type = NumResidualEvaluations
  [../]
  [./active_time]           # Time computer spent on simulation
    type = RunTime
    time_type = active
  [../]
  [./total_energy]          # Total free energy at each timestep
    type = ElementIntegralVariablePostprocessor
    variable = f_density
  [../]
```

```
[]

[Preconditioning]
  [./coupled]
    type = SMP
    full = true
  [../]
[]

[Executioner]
  type = Transient
  solve_type = NEWTON
  l_max_its = 30
  l_tol = 1e-6
  nl_max_its = 50
  nl_abs_tol = 2e-9
  end_time = 2419200
  petsc_options_iname = '-pc_type -ksp_grmres_restart -sub_ksp_type
                         -sub_pc_type -pc_asm_overlap'
  petsc_options_value = 'asm      31                 preonly
                         ilu          1'
  [./TimeStepper]
    type = IterationAdaptiveDT
    dt = 10
```

```
    cutback_factor = 0.8
    growth_factor = 1.5
    optimal_iterations = 7
  [../]
  [./Adaptivity]
    coarsen_fraction = 0.1
    refine_fraction = 0.7
    max_h_level = 2
  [../]
[]


[Debug]
  show_var_residual_norms = true
[]

[Outputs]
  exodus = true
  console = false
  csv = true
  [./console]
    type = Console
    max_rows = 10
  [../]
[]
```